Imperfections: using defects to program designer matter

Meeussen, A.S.

A. Appendices

A.1. Floppy motion of a triangular building block

The specific geometry of the triangular building block introduced in chapter 2, as shown in Fig. 2.1 and in Fig. A.1a, gives rise to a local floppy mode: the block can change its internal shape without deforming any of the rigid bonds. During this deformation, bonds pivot around the freely hinging nodes that connect them (Fig. A.1b).

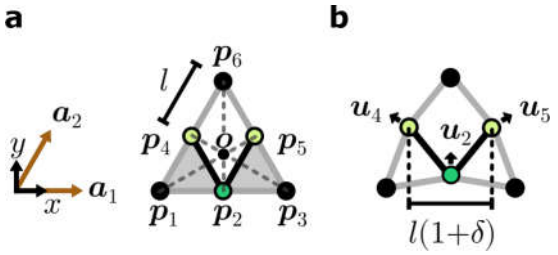

Fig. A.1.: Floppy motion of a building block. **a**, Anisotropic building block consisting of edge bonds (grey), internal bonds (black), corner nodes (black), majority edge-nodes (light green), and a minority edge-node (dark green). Node positions $\boldsymbol{p}$ are indicated in the xy-plane: the nodes are positioned at multiples of the lattice basis vectors $\boldsymbol{a}_1, \boldsymbol{a}_2$ with lattice constant l. **b**, Deformed building block in fat, expanded state. In the linear regime of small deformations, the edge-nodes move by a deflection $\boldsymbol{u}_i$. The two majority edge-nodes are separated by a length $l(1+\delta)$, where δ is a measure of block strain: it is positive for expansion (fat state) and negative for contraction (skinny state) of the block.

The positions $\{\boldsymbol{p}_i\}_{i=1}^6$ of the block's six nodes during the floppy deformation can be found via trigonometry. The deformation is prescribed by a single control parameter, the *block strain* $\delta \in [-1, 1]$ such that $l(1+\delta)$ encodes the distance between the two majority edge-nodes. The dimensionless quantity δ can be seen as a strain measure: positive δ indicate expansion of the block to a "fat" shape, associated with a positive block spin, while negative values signify contraction to a "thin" configuration with a negative block spin.

We calculate all node positions in units of the block's bond lengths l, which is set by the triangular basis vectors $\boldsymbol{a}_1 = l(1, 0)$ and $\boldsymbol{a}_2 = l(1/2, \sqrt{3}/2)$; the block's nodes are positioned at integer multiples of these vectors. The node positions as indicated in Fig. 2.1a are then given by the expressions below.

$$
\begin{aligned}
\boldsymbol{p}_1 &= \begin{pmatrix} -\frac{1}{2}\cos\theta - \frac{\sqrt{3}}{2}\sin\theta \\ \frac{\sqrt{3}}{2} - \frac{\sqrt{3}}{2}\cos\theta - \frac{1}{2}\sin\theta \end{pmatrix} & \boldsymbol{p}_2 &= \begin{pmatrix} 0 \\ \frac{\sqrt{3}}{2} - 2\sin\theta \end{pmatrix} \\
\boldsymbol{p}_3 &= \begin{pmatrix} \frac{1}{2}\cos\theta + \frac{\sqrt{3}}{2}\sin\theta \\ \frac{\sqrt{3}}{2} - \frac{\sqrt{3}}{2}\cos\theta - \frac{1}{2}\sin\theta \end{pmatrix} & \boldsymbol{p}_4 &= \begin{pmatrix} -\cos\theta \\ \frac{\sqrt{3}}{2} - \sin\theta \end{pmatrix} \\
\boldsymbol{p}_5 &= \begin{pmatrix} \cos\theta \\ \frac{\sqrt{3}}{2} - \sin\theta \end{pmatrix} & \boldsymbol{p}_6 &= \begin{pmatrix} 0 \\ \frac{\sqrt{3}}{2} \end{pmatrix},
\end{aligned}
\tag{A.1}
$$

where the equality $\delta = 2\cos\theta - 1$ has been used for legibility. Here, the origin of the xy-plane is chosen to lie at the centroid of the triangular block (see Fig. A.1a). In the linear regime of small shape changes such that $\delta << 1$, the node displacements $\{\boldsymbol{u}_i\}_{i=1}^6$, again

in units of bond length l, are determined up to rigid-body translations and rotations by:

$$\begin{aligned} \boldsymbol{u}_1 &= \begin{pmatrix} 0 \\ 0 \end{pmatrix} & \boldsymbol{u}_2 &= \begin{pmatrix} 0 \\ \frac{\delta}{\sqrt{3}} \end{pmatrix} \\ \boldsymbol{u}_3 &= \begin{pmatrix} 0 \\ 0 \end{pmatrix} & \boldsymbol{u}_4 &= \begin{pmatrix} -\frac{1}{2}\delta \\ \frac{1}{2\sqrt{3}}\delta \end{pmatrix} \\ \boldsymbol{u}_5 &= \begin{pmatrix} \frac{1}{2}\delta \\ \frac{1}{2\sqrt{3}}\delta \end{pmatrix} & \boldsymbol{u}_6 &= \begin{pmatrix} 0 \\ 0 \end{pmatrix}. \end{aligned} \tag{A.2}$$

In short, during the floppy deformation, the block's edge nodes move radially outward or inward from the triangle's centroid over a distance $\frac{\delta}{\sqrt{3}}$ during expansion or contraction.

A.2. Constructing delocalized SS-states

We show how to construct the $H_o - 1$ delocalized SS-states for any H-superhexagon metamaterial with $H_o > 1$ odd local loops. We consider the schematic shown in Fig. A.2, which illustrates how delocalized SS-states can be constructed iteratively. The network shown contains $H_o = 5$ odd local loops (numbered 1-5) that contains $H_o - 1 = 4$ delocalized SS-states (Fig. A.2a).

We first show how to create a delocalized SS-state running between a pair of two odd local loops (numbered 1, 2). We start by identifying a small subsection of the network to construct the SS-state in, consisting of the two incompatible superhexagons containing the odd local loops, and an arbitrary string of compatible superhexagons that connects the pair (Fig. A.2a, orange infill). We then transform this metamaterial strip into a compatible structure—in which all SS-states are known exactly—via a series of supertriangle rotations (Fig. A.2b, yellow triangles, arrows) that sequentially flip the parity of the local loops. We are left with a compatible structure in which all loop and radial SS-states are found by inspection (Fig. A.2c, radial SS-states not shown for clarity). As explained in Fig. 4.5e-g, these loop SS-states may then be recombined via sequential application of Eq. (4.4) under inversion of the applied supertriangle rotations, analogous to the construction discussed in Sec. 4.6.1. The linear combination of loop SS-states thus produces a delocalized SS-state of the metamaterial strip with the two odd local loops 1 and 2 (Fig. A.2d, arrows).

In a metamaterial with H_o odd loops, we can find $H_o - 1$ independent delocalized states using the above procedure. Independence is ensured by selecting $H_o - 1$ independent pairs of incompatible superhexagons (such that each is selected at least once), with strings of compatible superhexagons running between them. Figure A.2e demonstrates the three remaining delocalized SS-states found between defect pairs $(2, 3)$, $(3, 4)$, and $(4, 5)$ in our example.

It should be noted that the delocalized states are not unique: their shape depends on the path between each defect pair, and the choice of supertriangle rotations. However, the space spanned by the resulting basis of SS-states does not depend on the path choice. In particular, this procedure renders an independent, non-orthogonal set of $H_o - 1$ delocalized SS-states. Together with the known radial and loop SS-states, which are identified by inspection, a complete and independent basis of SS-space can be found for our metamaterials with any defect configuration.

A.3. Evolution of LB-spaces under architectural transformations

In Sec. 4.6, we discussed the evolution of a metamaterial's stress space (consisting of the SS- and complementary LB-space) under architectural transformations. We demonstrated that the evolution of the SS-space is limited to one, two, or no changing SS-states for distinct types of supertriangle rotations, denoted process I, process II, and process III, respectively. Here, we derive the concomitant evolution of the metamaterial's LB-space for all three processes.

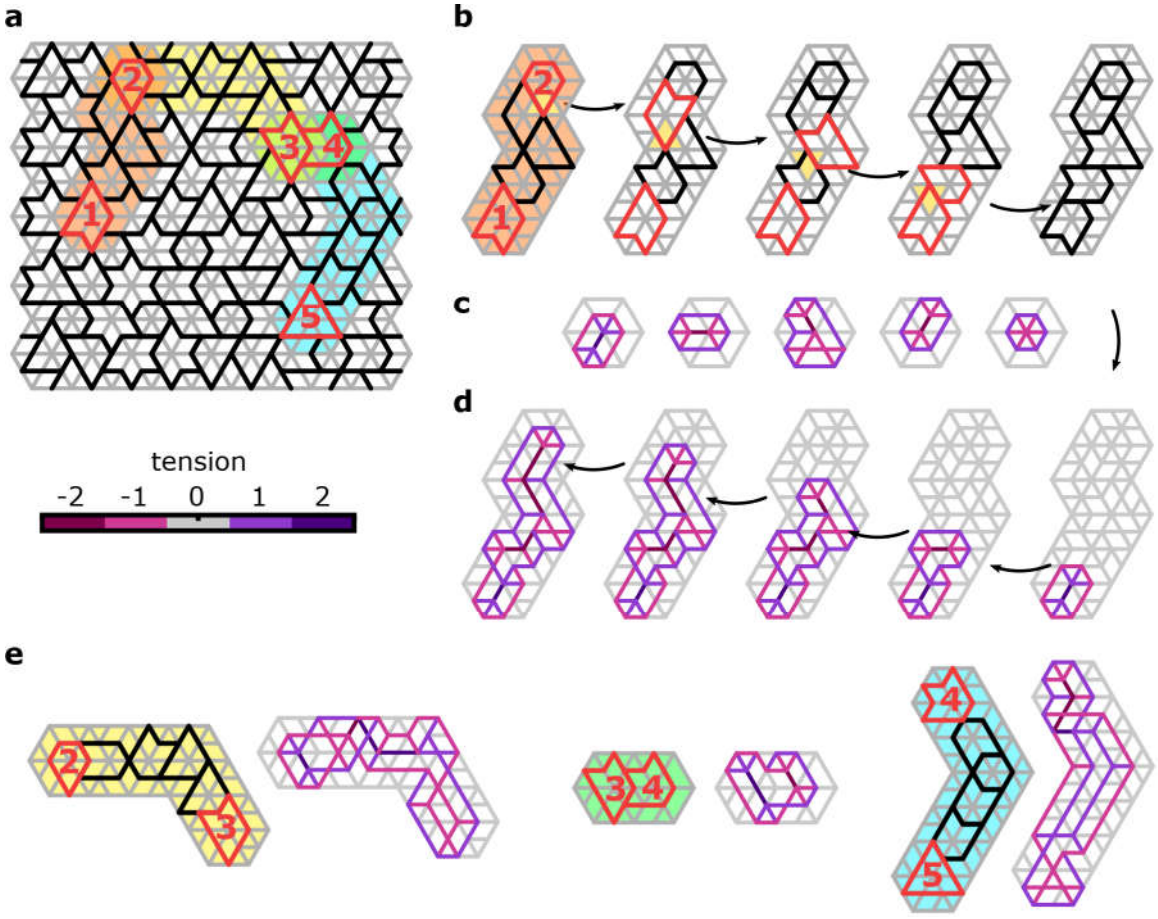

Fig. A.2.: a, An incompatible metamaterial architecture containing $H_o = 5$ odd local loops (numbers 1-5, red bold lines) and $H - H_0 = 72$ even ones (black bold lines). The metamaterial contains $H_o - 1 = 4$ delocalized SS-states, which are constructed on metamaterial paths connecting four independent pairs of incompatible hexagons (infills in orange, 1-2; yellow, 2-3; green, 3-4; and blue, 4-5). **b**, The incompatible metamaterial strip between superhexagons 1,2 is made compatible by sequential supertriangle rotations (yellow triangles, arrows) that change the parity of local loops. **c**, The compatible metamaterial's SS-states are spanned by radial (not shown) and loop SS-states (colour bar). **d**, The loop SS-states are recombined into a delocalized SS-state of the incompatible metamaterial strip using Eq. (4.4) (arrows), yielding a delocalized SS-state between the incompatible superhexagons 1 and 2. **e**, With the procedure demonstrated in b—d, the other three delocalized SS-states are constructed between the remaining pairs of odd local loops.

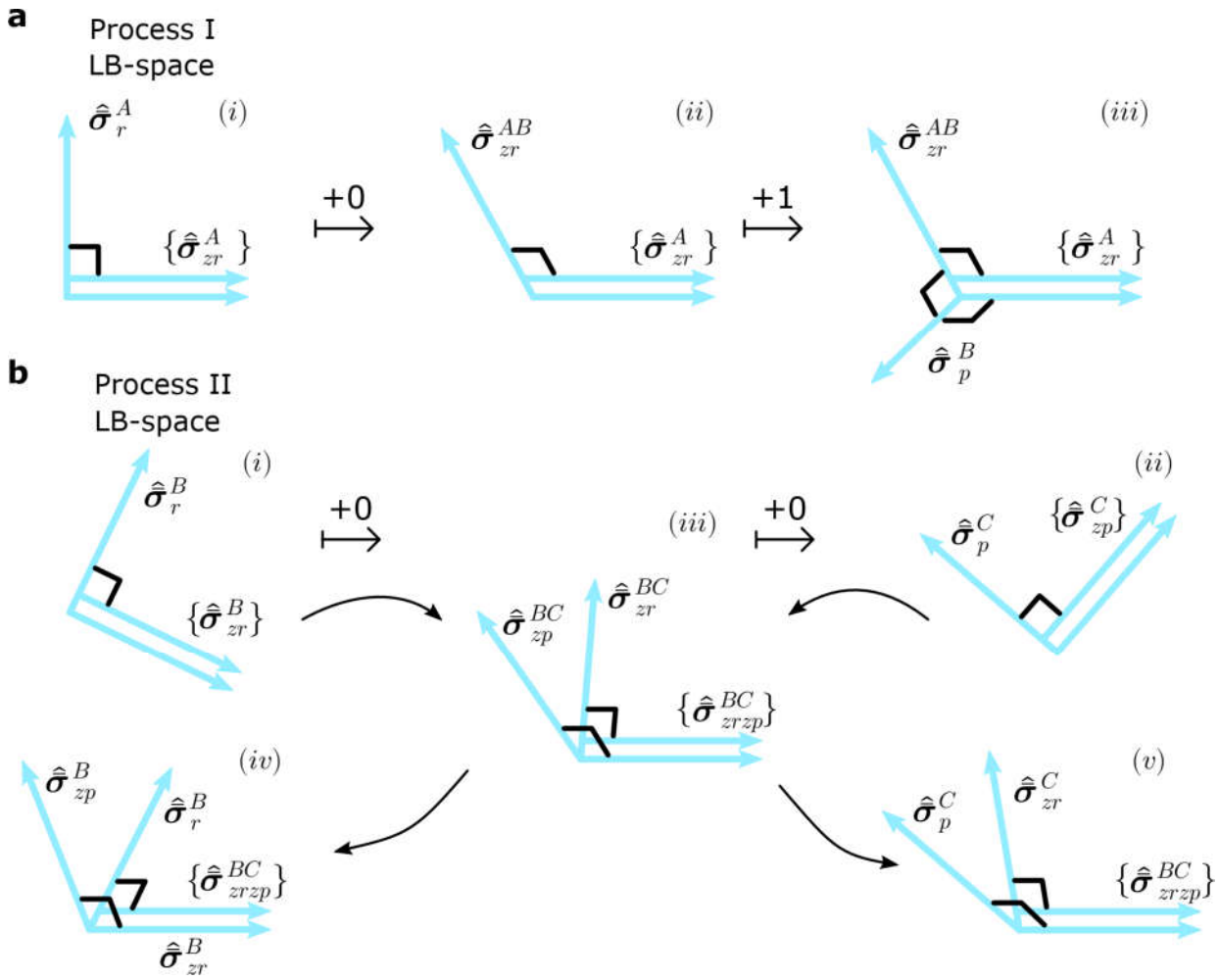

Fig. A.3.: Evolution of the LB-space under a supertriangle rotation according to processes I and II. **a**, Process I: a compatible network A is transformed to an incompatible network B via an intermediate network AB, by first removing bond r and then adding bond p (see Fig. 4.7). For network A, we construct an orthogonal basis for the LB-space that contains those states $\{\hat{\tilde{\boldsymbol{\sigma}}}^A_{zr}\}$ that remain in network AB as well as B. The full bases of networks A and B additionally contain a state that is added ($\hat{\tilde{\boldsymbol{\sigma}}}^B_p$) and a state that is modified ($\hat{\tilde{\boldsymbol{\sigma}}}^A_r$ to $\hat{\tilde{\boldsymbol{\sigma}}}^{AB}_{zr}$) during the architectural transformation; for details on the execution of steps *(i)-(iii)*, see text. **b**,Process II: an incompatible network B is transformed to an incompatible network C via an intermediate network BC, by first removing bond r and then adding bond p (see Fig. 4.8). For network B (P), we construct an orthogonal basis for the LB-space that contains states $\{\hat{\tilde{\boldsymbol{\sigma}}}^B_{zr}\}$ ($\{\hat{\tilde{\boldsymbol{\sigma}}}^C_{zp}\}$) without stress on r (p), and $\hat{\tilde{\boldsymbol{\sigma}}}^B_r$ ($\hat{\tilde{\boldsymbol{\sigma}}}^C_p$) with finite stress there. We construct a suitable basis of LB-space for the intermediate network BC (with no stress on p or r) via an orthogonalization procedure, which produces LB-states $\{\hat{\tilde{\boldsymbol{\sigma}}}^{BC}_{zrzp}\}$ that are shared with networks B and C, and states $\hat{\tilde{\boldsymbol{\sigma}}}^{BC}_{zp}$, $\hat{\tilde{\boldsymbol{\sigma}}}^{BC}_{zr}$ that are modified to states $\hat{\tilde{\boldsymbol{\sigma}}}^B_{zp}$ and $\hat{\tilde{\boldsymbol{\sigma}}}^C_{zr}$ in networks B and C respectively. For details on the execution of steps *(i)-(v)*, see text. Black squares signify orthogonality, and arrows with numbers indicate changes in the dimensions of the LB-space.

A.3.1. Process I: compatible to incompatible metamaterial

We describe the evolution of the LB-space when a compatible network A is transformed into an incompatible network B; this evolution is shown schematically in Fig. A.3a. The architectural transformation occurs via a supertriangle rotation that removes a bond r and adds a bond p (see Fig. 4.7a). The LB-space evolution is closely related to the evolution of the SS-space discussed in Sec. 4.6.2 (see Fig. 4.7b), and involves three separate calculations *(i)-(iii)* below.

(i) We aim to construct a basis for the LB-space of network A that consists of one LB-state, $\hat{\bar{\boldsymbol{\sigma}}}_r^A$, that has a finite stress on bond r, and a remaining set of orthogonal vectors $\{\hat{\bar{\boldsymbol{\sigma}}}_{zr}^A\}$ that have zero stress om bond r (Fig. 4.7c, left). Under removal of bond r, only the LB-state $\hat{\bar{\boldsymbol{\sigma}}}_r^A$ will be modified. Since the set $\{\hat{\bar{\boldsymbol{\sigma}}}_{zr}^A\}$ is unaffected by removing r and adding p, we do not need to construct it explicitly, and focus on identifying $\hat{\bar{\boldsymbol{\sigma}}}_r^A$ instead. To construct this unique LB-state with nonzero stress on bond r, note that the stress state $\hat{\boldsymbol{r}}$ must be a linear combination of the SS-state $\hat{\bar{\boldsymbol{\tau}}}_r^A$ (see Sec. 4.6.2) and $\hat{\bar{\boldsymbol{\sigma}}}_r^A$—the only two stress states with nonzero stress on r—and since $\hat{\bar{\boldsymbol{\tau}}}_r^A$ and $\hat{\bar{\boldsymbol{\sigma}}}_r^A$ are perpendicular, we find

$$\hat{\bar{\boldsymbol{\sigma}}}_r^A \propto \mathrm{Rej}(\hat{\boldsymbol{r}}, \hat{\bar{\boldsymbol{\tau}}}_r^A) \,, \tag{A.3}$$

as shown in Fig. A.3a, left. Here, we define the vector rejection Rej( ) to be the complement of vector projection: $\mathrm{Proj}(\boldsymbol{u}, \boldsymbol{v}) = \frac{\boldsymbol{u}\cdot\boldsymbol{v}}{\boldsymbol{v}\cdot\boldsymbol{v}}\boldsymbol{v}$ and $\boldsymbol{u} = \mathrm{Proj}(\boldsymbol{u}, \boldsymbol{v}) + \mathrm{Rej}(\boldsymbol{u}, \boldsymbol{v})$, so that $\mathrm{Rej}(\boldsymbol{u}, \boldsymbol{v}) := \boldsymbol{u} - \frac{\boldsymbol{u}\cdot\boldsymbol{v}}{\boldsymbol{v}\cdot\boldsymbol{v}}\boldsymbol{v}$.

(ii) When bond r is removed from network A, the LB-state $\hat{\bar{\boldsymbol{\sigma}}}_r^A$ must disappear; the LB-states $\{\hat{\bar{\boldsymbol{\sigma}}}_{zr}^A\}$ remain. However, as the number of LB-states in AB is the same as in network A (see above), the intermediate network AB must contain a new LB-state, $\hat{\bar{\boldsymbol{\sigma}}}_{zr}^{AB}$, with zero stress on bond r. This state must be perpendicular to the SS-space spanned by $\{\hat{\bar{\boldsymbol{\tau}}}_{zr}^A\}$, and to the LB-states $\{\hat{\bar{\boldsymbol{\sigma}}}_{zr}^A\}$. However, $\hat{\bar{\boldsymbol{\sigma}}}_{zr}^{AB}$ does not need to be perpendicular to the state $\hat{\bar{\boldsymbol{\tau}}}_r^A$, so that we can construct $\hat{\bar{\boldsymbol{\sigma}}}_{zr}^{AB}$ from the states $\hat{\bar{\boldsymbol{\tau}}}_r^A$ and $\hat{\boldsymbol{r}}$:

$$\hat{\bar{\boldsymbol{\sigma}}}_{zr}^{AB} \propto Rej(\hat{\bar{\boldsymbol{\tau}}}_r^A, \hat{\boldsymbol{r}}) \,, \tag{A.4}$$

as shown in Fig. A.3a, middle.

(iii) Finally, when network AB evolves to network B by adding bond p, a new LB-state $\hat{\bar{\boldsymbol{\sigma}}}_p^B$ must appear. The new LB-state is perpendicular to both the SS-space spanned by $\{\hat{\bar{\boldsymbol{\tau}}}_{zr}^A\}$ as well as the LB-space spanned by $\{\{\hat{\bar{\boldsymbol{\sigma}}}_{zr}^A\}, \hat{\bar{\boldsymbol{\sigma}}}_{zr}^{AB}\}$, and has a finite stress on bond p. It is easy to check that the stress state $\hat{\boldsymbol{p}}$ uniquely satisfies these criteria: $\hat{\bar{\boldsymbol{\sigma}}}_p^B = \hat{\boldsymbol{p}}$ (Fig. A.3a, right).

In summary, as we illustrate in Fig. A.3a and Fig. 4.7, the stress spaces of architecturally related networks A and B are identical up to the following four independent vectors: the SS-state $\hat{\bar{\boldsymbol{\tau}}}_r^A$, present in network A, but not in B; the LB-state $\hat{\boldsymbol{p}}$, present in B but not in A; and the LB-state $\hat{\bar{\boldsymbol{\sigma}}}_r^A$ in network A that changes to the LB-state $\hat{\bar{\boldsymbol{\sigma}}}_{zr}^{AB}$ in network B. These four independent vectors are spanned by the set $\{\hat{\bar{\boldsymbol{\tau}}}_r^A, \hat{\boldsymbol{r}}, \hat{\boldsymbol{p}}\}$ consisting of the mutated SS-state and the pure stress vectors on bonds p and r.

A.3.2. Process II: incompatible to incompatible metamaterial

We now describe the evolution of the LB-space when an incompatible network B is transformed into a distinct incompatible network C as shown in Fig. A.3b, via a supertriangle rotation that removes a bond r and adds a bond p (see Fig. 4.8a). This evolution is closely related to the evolution of the SS-space discussed in Sec. 4.6.3 (see Fig. 4.8b), and involves five separate calculations *(i)*-*(v)* below.

We can construct the LB-spaces of networks B and C, analogous to step *(ii)* in process I. This readily yields bases *(i)* $\{\{\hat{\boldsymbol{\sigma}}^B_{zr}\}, \hat{\boldsymbol{\sigma}}^B_r\}$ and *(ii)* $\{\{\hat{\boldsymbol{\sigma}}^C_{zp}\}, \hat{\boldsymbol{\sigma}}^C_p\}$ (Fig. A.3b, left and right). However, as the sets $\{\hat{\boldsymbol{\sigma}}^B_{zr}\}$ and $\{\hat{\boldsymbol{\sigma}}^C_{zp}\}$ are not the same, the bases are not suitable to compare the LB-spaces.

(iii) We now construct an appropriate basis for the LB-space of network BC, which contains a set $\{\hat{\boldsymbol{\sigma}}^{BC}_{zrzp}\}$ that is shared with the LB-spaces of network B and C (Fig. A.3b, middle). First, we can start from the LB-basis *(i)*, remove bond r, and analogous to step *(ii)* of process I, obtain a basis $\{\{\hat{\boldsymbol{\sigma}}^B_{zr}\}, \hat{\boldsymbol{\sigma}}^{BC}_{zr}\}$. Second, starting from the LB-basis *(ii)* and removing bond p we obtain a basis $\{\{\hat{\boldsymbol{\sigma}}^C_{zp}\}, \hat{\boldsymbol{\sigma}}^{BC}_{zp}\}$. These two bases both span the LB-space of network BC. We now use this to construct the appropriate basis of the LB-space, $\{\hat{\boldsymbol{\sigma}}^{BC}_{zp}, \hat{\boldsymbol{\sigma}}^{BC}_{zr}, \{\hat{\boldsymbol{\sigma}}^{BC}_{zpzr}\}\}$, so that the set $\{\hat{\boldsymbol{\sigma}}^{BC}_{zpzr}\}$ is shared with the LB-spaces of network B and C. We first perform a Gram-Schmidt process on the ordered set $\{\hat{\boldsymbol{\sigma}}^{BC}_{zp}, \hat{\boldsymbol{\sigma}}^{BC}_{zr}, \{\hat{\boldsymbol{\sigma}}^{B}_{zr}\}\}$, and then define $\{\hat{\boldsymbol{\sigma}}^{BC}_{zpzr}\}$ as the last $N_b - 2H - 1$ vectors of the resulting orthonormal basis. To facilitate comparison with networks B and C, we obtain a full LB-space basis of network BC by adding the vectors $\hat{\boldsymbol{\sigma}}^{BC}_{zp}$ and $\hat{\boldsymbol{\sigma}}^{BC}_{zr}$, so that all but the first two basis vectors are orthogonal.

We now obtain appropriate bases for the LB-spaces of networks B and C as follows (see Fig. A.3b, left and right).

(iv) We construct a basis for the LB-space of network B by ensuring the orthogonality of the LB-space basis of network BC, $\{\hat{\boldsymbol{\sigma}}^{BC}_{zp}, \hat{\boldsymbol{\sigma}}^{BC}_{zr}, \{\hat{\boldsymbol{\sigma}}^{BC}_{zpzr}\}\}$, with the SS-space of network B. We do this by rejecting each vector on the SS-state $\hat{\bar{\boldsymbol{\tau}}}^B_r$, that is present in network B but not in BC. This rejection procedure results in an LB-space basis of network B: $\{\hat{\boldsymbol{\sigma}}^B_{zp}, \hat{\boldsymbol{\sigma}}^B_r, \{\hat{\boldsymbol{\sigma}}^{BC}_{zpzr}\}\}$.

(v) A similar procedure results in an analogous LB-space basis for network C: $\{\hat{\boldsymbol{\sigma}}^C_{zr}, \hat{\boldsymbol{\sigma}}^C_p, \{\hat{\boldsymbol{\sigma}}^{BC}_{zpzr}\}\}$.

In summary, as shown in Fig. A.3b and Fig. 4.8, the stress spaces of architecturally related networks B and C are identical up to the following vectors: the SS-state $\hat{\bar{\boldsymbol{\tau}}}^B_r$, present in network B, but not in C; the SS-state $\hat{\bar{\boldsymbol{\tau}}}^C_p$, present in network C, but not in B (see Sec. 4.6.3); the LB-state $\hat{\boldsymbol{\sigma}}^B_r$ in network B that changes to the LB-state $\hat{\boldsymbol{\sigma}}^C_{zr}$ in network C; and the LB-state $\hat{\boldsymbol{\sigma}}^C_p$ in network C that changes to the LB-state $\hat{\boldsymbol{\sigma}}^B_{zp}$ in network B. These four independent vectors are spanned by the set $\{\hat{\bar{\boldsymbol{\tau}}}^B_r, \hat{\bar{\boldsymbol{\tau}}}^C_p, \hat{\boldsymbol{r}}, \hat{\boldsymbol{p}}\}$ consisting of the mutated SS-states and the pure stress vectors on bonds p and r.

A.3.3. Process III: compatible to compatible metamaterial

A compatible network A may be transformed to a distinct compatible network A' by some supertriangle rotations that remove a bond r and add a bond p. Only supertriangle rotations at the system's edge that do not change the parity of any local loops (see Sec. 4.5) can generate such a network pair. By construction, these special architectural transformations do not change the shape of any local loops, and thus do not affect the SS-space (see Sec. 4.6.1). As a consequence, under an externally applied load that is supported by both networks A and A', the stress response of both networks must be identical. Since only the bonds r and p differ between the two networks, the stress spaces of networks A and A' are identical up to the following vectors: the LB-state $\hat{\bar{\boldsymbol{\sigma}}}_r^A = \hat{\boldsymbol{r}}$, present in network A but not in A', and the LB-state $\hat{\bar{\boldsymbol{\sigma}}}_p^{A'} = \hat{\boldsymbol{p}}$, present in A' but not in A. Since the stress response to external loading that is supported by both networks must be identical, the LB-states $\hat{\boldsymbol{r}}$ and $\hat{\boldsymbol{p}}$ will therefore not contribute to the network's mutual supported stress responses: the bonds r and p remain unstressed.

A.4. Mechanical interpretation of evolving LB-states

Having discussed the evolution of LB-space under supertriangle rotations in Appendix A.3, we now present the mechanical interpretation of the mutated LB-states. We show here that the few stress states that are added, removed, or modified in processes I and II (Secs. 4.6.2 and 4.6.3) correspond to the metamaterials' stress response to well-defined external nodal loads. In particular, we show below that all mutated LB-states correspond to nodal load dipoles along the two bonds r, p that are mutually exclusive between the post- and pre-transformation networks. A nodal load dipole generates equal and opposite forces at two nodes, and is oriented along the connecting line between the two nodes. The mutating LB-states either generate a large stress on a single bond and a diffuse field around it, or an extended stress field around a missing bond, as illustrated in Fig. A.4.

We first consider the stress response evolution of process I, when a compatible material A is transformed into an incompatible material B (Fig. A.4a). During this transformation, the LB-state $\bar{\boldsymbol{\sigma}}_r^A$ of network A changes. The physical interpretation of this stress state is as follows. The state $\bar{\boldsymbol{\sigma}}_r^A$ is a linear combination of the SS-state $\hat{\bar{\boldsymbol{\tau}}}_r^A$ and the unit bond stress $\hat{\boldsymbol{r}}$, such that the final LB-state is orthogonal to the SS-state (Eq. (A.3)). The unit bond stress corresponds via Hooke's law to a nodal load dipole $\sqrt{2}\hat{\boldsymbol{f}}_r$: that is, the two nodes connected by bond r undergo an equal and opposite force, extending the bond (here, the prefactor $\sqrt{2}$ is a consequence of normalization). The SS-state, by definition, generates no nodal loads. Thus, the stress state $\bar{\boldsymbol{\sigma}}_r^A$ in network A must map to the nodal load state $\sqrt{2}\hat{\boldsymbol{f}}_r$:

$$\bar{\boldsymbol{\sigma}}_r^A = \hat{\boldsymbol{r}} - (\hat{\boldsymbol{r}} \cdot \hat{\bar{\boldsymbol{\tau}}}_r^A)\hat{\bar{\boldsymbol{\tau}}}_r^A \leftrightarrow \sqrt{2}\hat{\boldsymbol{f}}_r \tag{A.5}$$

In network B, the LB-state $\bar{\boldsymbol{\sigma}}_r^A$ is replaced by a new LB-state $\bar{\boldsymbol{\sigma}}_{zr}^{AB}$. It is a linear combination of the SS-state $\hat{\bar{\boldsymbol{\tau}}}_r^A$ and the unit bond stress $\hat{\boldsymbol{r}}$ such that any stress on r is cancelled out (see Eq. (A.4)). Here, again, the unit bond stress $\hat{\boldsymbol{r}}$ maps to the nodal load $\sqrt{2}\hat{\boldsymbol{f}}_r$, while the SS-state $\hat{\bar{\boldsymbol{\tau}}}_r^A$ generates no load. Hence, in network B,

$$\bar{\boldsymbol{\sigma}}_{zr}^{AB} = \hat{\boldsymbol{r}} - \frac{1}{\hat{\boldsymbol{r}} \cdot \hat{\bar{\boldsymbol{\tau}}}_r^A}\hat{\bar{\boldsymbol{\tau}}}_r^A \leftrightarrow \sqrt{2}\hat{\boldsymbol{f}}_r \ . \tag{A.6}$$

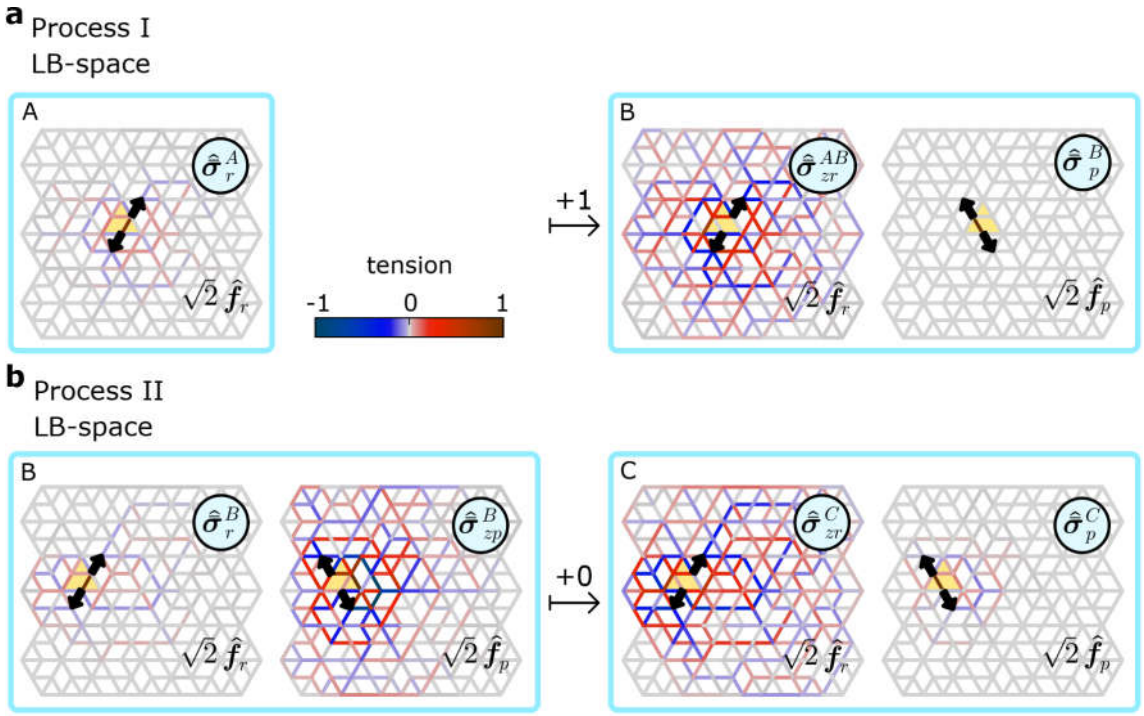

Fig. A.4.: Mechanical interpretation of the LB-states that change under a supertriangle rotation for processes I and II. **a**, A compatible network A transforms into an incompatible network B according to process I. One LB-state $\hat{\tilde{\boldsymbol{\sigma}}}_r^A$ (colour bar) changes to $\hat{\tilde{\boldsymbol{\sigma}}}_{zr}^{AB}$ under the transformation; both LB-states map to the same nodal load dipole $\sqrt{2}\hat{\boldsymbol{f}}_r$ along bond r (arrows). One LB-state $\hat{\tilde{\boldsymbol{\sigma}}}_p^B$ is added in network B: it maps to the nodal load dipole $\sqrt{2}\hat{\boldsymbol{f}}_p$ along bond p, which load is not supported in network A. **b**, An incompatible network B transforms into an incompatible network C according to process II. The LB-state $\hat{\tilde{\boldsymbol{\sigma}}}_r^B$ in network B changes to $\hat{\tilde{\boldsymbol{\sigma}}}_{zr}^C$ in network C. Both LB-states map to the same nodal load dipole $\sqrt{2}\hat{\boldsymbol{f}}_r$ along bond r (arrows). In addition, the LB-state $\hat{\tilde{\boldsymbol{\sigma}}}_p^C$ in network C changes to $\hat{\tilde{\boldsymbol{\sigma}}}_{zp}^B$ in network B. Both LB-states map to the same nodal load dipole $\sqrt{2}\hat{\boldsymbol{f}}_p$ along bond p (arrows).

Lastly, process I introduces a new LB-state $\hat{\bar{\boldsymbol{\sigma}}}_p^B = \hat{\boldsymbol{p}}$ in network B. Using the same arguments as above, we find that the new LB-state corresponds to a load dipole $\sqrt{2}\hat{\boldsymbol{f}}_p$ along bond p:

$$\bar{\boldsymbol{\sigma}}_p^B = \hat{\boldsymbol{p}} \leftrightarrow \sqrt{2}\hat{\boldsymbol{f}}_p \ . \tag{A.7}$$

This LB-state has no counterpart in network A: there, the nodal load $\sqrt{2}\hat{\boldsymbol{f}}_p$ activates the compatible material's floppy mode, and is not supported. The remaining LB-states $\{\hat{\bar{\boldsymbol{\sigma}}}_{zr}^A\}$, that are shared between networks A and B, are unchanged; they map to identical loads in both networks. An overview of the mutated LB-states, and the nodal loads corresponding to the latter, is shown in Fig. A.4a.

Secondly, we treat the stress response evolution of process II, where an incompatible material B is mutated into an incompatible material C (Fig. A.4b). There are two LB-states that are modified during this transformation: $\hat{\bar{\boldsymbol{\sigma}}}_r^B$ and $\hat{\tilde{\bar{\boldsymbol{\sigma}}}}_{zp}^{BC}$ in network B are changed into $\hat{\bar{\boldsymbol{\sigma}}}_p^C$ and $\hat{\tilde{\bar{\boldsymbol{\sigma}}}}_{zr}^{BC}$ in network C. Using an analogous argument as for process I, the LB-state $\hat{\bar{\boldsymbol{\sigma}}}_r^B$ in network B maps to the nodal load $\sqrt{2}\hat{\boldsymbol{f}}_r$:

$$\bar{\boldsymbol{\sigma}}_r^B = \hat{\boldsymbol{r}} - (\hat{\boldsymbol{r}} \cdot \hat{\bar{\boldsymbol{\tau}}}_r^B)\hat{\bar{\boldsymbol{\tau}}}_r^B \leftrightarrow \sqrt{2}\hat{\boldsymbol{f}}_r \tag{A.8}$$

In intermediate network BC:

$$\bar{\boldsymbol{\sigma}}_{zr}^{BC} = \hat{\boldsymbol{r}} - \frac{1}{\hat{\boldsymbol{r}} \cdot \hat{\bar{\boldsymbol{\tau}}}_r^B}\hat{\bar{\boldsymbol{\tau}}}_r^B \leftrightarrow \sqrt{2}\hat{\boldsymbol{f}}_r \tag{A.9}$$

and finally in network C:

$$\bar{\boldsymbol{\sigma}}_{zr}^C = \mathrm{Rej}(\bar{\boldsymbol{\sigma}}_{zr}^{BC}, \hat{\bar{\boldsymbol{\tau}}}_p^C) = \hat{\boldsymbol{r}} - \frac{\hat{\bar{\boldsymbol{\tau}}}_r^B - (\hat{\bar{\boldsymbol{\tau}}}_r^B \cdot \hat{\bar{\boldsymbol{\tau}}}_p^C)\hat{\bar{\boldsymbol{\tau}}}_p^C}{\hat{\boldsymbol{r}} \cdot \hat{\bar{\boldsymbol{\tau}}}_r^B} \leftrightarrow \sqrt{2}\hat{\boldsymbol{f}}_r \tag{A.10}$$

Similarly, the LB-state $\hat{\bar{\boldsymbol{\sigma}}}_p^C$ maps to the nodal load $\sqrt{2}\hat{\boldsymbol{f}}_p$ in network C:

$$\bar{\boldsymbol{\sigma}}_p^C = \hat{\boldsymbol{p}} - (\hat{\boldsymbol{p}} \cdot \hat{\bar{\boldsymbol{\tau}}}_p^C)\hat{\bar{\boldsymbol{\tau}}}_p^C \leftrightarrow \sqrt{2}\hat{\boldsymbol{f}}_p \tag{A.11}$$

In intermediate network BC:

$$\bar{\boldsymbol{\sigma}}_{zp}^{BC} = \hat{\boldsymbol{p}} - \frac{1}{\hat{\boldsymbol{p}} \cdot \hat{\bar{\boldsymbol{\tau}}}_p^C}\hat{\bar{\boldsymbol{\tau}}}_p^C \leftrightarrow \sqrt{2}\hat{\boldsymbol{f}}_p \tag{A.12}$$

and finally in network B:

$$\bar{\boldsymbol{\sigma}}_{zp}^B = \mathrm{Rej}(\bar{\boldsymbol{\sigma}}_{zp}^{BC}, \hat{\bar{\boldsymbol{\tau}}}_r^B) = \hat{\boldsymbol{p}} - \frac{\hat{\bar{\boldsymbol{\tau}}}_p^C - (\hat{\bar{\boldsymbol{\tau}}}_p^C \cdot \hat{\bar{\boldsymbol{\tau}}}_r^B)\hat{\bar{\boldsymbol{\tau}}}_r^B}{\hat{\boldsymbol{p}} \cdot \hat{\bar{\boldsymbol{\tau}}}_p^C} \leftrightarrow \sqrt{2}\hat{\boldsymbol{f}}_p \tag{A.13}$$

The remaining LB-states $\{\hat{\bar{\boldsymbol{\sigma}}}_{zrzp}^{BC}\}$ are unmodified and map to the same nodal loads in both networks. The mutated LB-states are illustrated in Fig. A.4b.

Lastly, we discuss the stress response evolution for process III, where a compatible material A transforms to a distinct compatible material A'There are two LB-states that are modified during this transformation: $\hat{\boldsymbol{r}}$ and $\hat{\boldsymbol{p}}$ are mutually exclusive LB-states of networks A and A' respectively. Using similar arguments as above, the LB-state $\hat{\boldsymbol{r}}$ in

network A maps to the nodal load dipole $\sqrt{2}\hat{\boldsymbol{f}}_r$:

$$\hat{\boldsymbol{r}} \leftrightarrow \sqrt{2}\hat{\boldsymbol{f}}_r \tag{A.14}$$

This load dipole is not supported in network A'—it activates the global floppy mode of the system—and there is no counterpart to the LB-state $\hat{\boldsymbol{r}}$ in network A'. Analogously, in network A',

$$\hat{\boldsymbol{p}} \leftrightarrow \sqrt{2}\hat{\boldsymbol{f}}_p \ , \tag{A.15}$$

and this LB-state in network A', being unsupported by network A, has no counterpart in the LB-space of A.

A.5. Derivation of stress response differences

With our description of the stress space evolution and its physical interpretation in Appendices A.3 and A.4, we are now in a position to derive exactly how a metamaterial's stress response under external loading changes when its architecture is changed by rotating a supertriangle. In particular, we found that the SS-space of two networks related by a single supertriangle rotation are identical up to at most two mutually exclusive SS-states. Comparing two networks, related by a supertriangle rotation, by calculating their stress response difference $\Delta\boldsymbol{\sigma}$ under identical supported loads, we will now show that $\Delta\boldsymbol{\sigma}$ is a linear combination of only those SS-states that have been changed by the network's architectural transformation.

In any network, the stress response $\boldsymbol{\sigma}$ to an arbitrary supported load $\boldsymbol{f}$ can be written as a unique linear combination of LB-states: $\boldsymbol{\sigma} = \sum_{i=1} (C_i \boldsymbol{\sigma}_i)$, where the set $\{\boldsymbol{\sigma}_i\}$ is any linearly independent basis of stress vectors spanning the LB-space, and the coefficients C_i depend on the applied load, the material's geometry, and the choice of basis. The exact coefficients can be calculated using the matrix formalism discussed in Sec. 4.2. We use this representation to find an expression for the stress response difference between two networks, related via process I, II, or III, under identical supported loads.

We first consider networks A and B, related via process I. When structure A is subjected to a supported load $\boldsymbol{f}$—that is, a load that does not excite the FM of network A—the stress response $\boldsymbol{\sigma}^A$ is written in a straightforward way:

$$\boldsymbol{\sigma}^A = \sum_{i=1}^{N_b-2H-1} \left(C_i \hat{\bar{\boldsymbol{\sigma}}}^A_{zr,i} \right) + C_r \bar{\boldsymbol{\sigma}}^A_r \ , \tag{A.16}$$

where we have chosen a basis of LB-space such that the LB-states $\{\hat{\bar{\boldsymbol{\sigma}}}^A_{zr}\}$ are shared between the two networks, and the LB-state $\bar{\boldsymbol{\sigma}}^A_r$ is unique to network A (see Appendix A.3). As discussed in Appendix A.4, when a supertriangle is rotated in network A to produce network B, the nodal load dipole generated by the stress state $\bar{\boldsymbol{\sigma}}^A_r$ in network A is supported instead by the stress state $\bar{\boldsymbol{\sigma}}^{AB}_{zr}$ in network B; in addition, the basis of LB-space now contains an extra LB-state $\hat{\boldsymbol{p}}$ that maps to a load dipole along bond p. For network B, the stress response to the same external loading $\boldsymbol{f}$ is then written as:

$$\boldsymbol{\sigma}^B = \sum_{i=1}^{N_b-2H-1} \left(C_i \hat{\bar{\boldsymbol{\sigma}}}^A_{zr,i} \right) + C_r \bar{\boldsymbol{\sigma}}^{AB}_{zr} + C_p \hat{\boldsymbol{p}} \ . \tag{A.17}$$

Comparing Eqs. (A.16) and (A.17), we note that the LB-states $\{\hat{\bar{\boldsymbol{\sigma}}}^{A}_{zr,i}\}$ are shared between networks A and B, and map to identical loads, so that the coefficients C_i are equal. Furthermore, $C_a = 0$ by necessity, since the load dipole along bond p excites the FM of network A and cannot be part of our load $\boldsymbol{f}$, which must be supported by both networks. Lastly, the stress field $\bar{\boldsymbol{\sigma}}^{AB}_{zr}$ corresponds to the stress field $\bar{\boldsymbol{\sigma}}^{A}_{r}$—both mapping to the load dipole $\sqrt{2}\hat{\boldsymbol{f}}_r$—so that the coefficient C_r in both equations is equal. Using Eqs. (A.5-A.6) and Eqs. (A.16-A.17), we find the following expression for the stress response difference between networks A and B:

$$\Delta\boldsymbol{\sigma} = \boldsymbol{\sigma}^{B} - \boldsymbol{\sigma}^{A} = C_r \frac{-1 + (\hat{\boldsymbol{r}} \cdot \hat{\bar{\boldsymbol{\tau}}}^{A}_{r})^2}{\hat{\boldsymbol{r}} \cdot \hat{\bar{\boldsymbol{\tau}}}^{A}_{r}} \hat{\bar{\boldsymbol{\tau}}}^{A}_{r} \in \mathrm{Sp}(\hat{\bar{\boldsymbol{\tau}}}^{A}_{1}) \ . \tag{A.18}$$

Eq. (A.18) shows that the stress response difference between the two networks is parallel to the single mutated SS-state $\hat{\bar{\boldsymbol{\tau}}}^{A}_{r}$. We confirm this finding via numerical calculations: the stress response difference between network A with no defect and network B with a structural defect, illustrated in Fig. 4.1a (right) corresponds exactly to the lost state of self stress shown in Fig. 4.9b (top), resulting in a differential stress response that is localized near the defect.

A similar procedure allows us to find the stress response difference between two distinct incompatible networks B and C, related via process II. The stress response of network B may be written as:

$$\boldsymbol{\sigma}^{B} = \sum_{i=1}^{N_b - 2H - 1} \left(C_i \hat{\bar{\boldsymbol{\sigma}}}^{BC}_{zpzr,i} \right) + C_r \bar{\boldsymbol{\sigma}}^{B}_{r} + C_p \bar{\boldsymbol{\sigma}}^{B}_{zp} \ , \tag{A.19}$$

while the stress response of network C is given by:

$$\boldsymbol{\sigma}^{B} = \sum_{i=1}^{N_b - 2H - 1} \left(C_i \hat{\bar{\boldsymbol{\sigma}}}^{BC}_{zpzr,i} \right) + C_r \bar{\boldsymbol{\sigma}}^{C}_{zr} + C_p \bar{\boldsymbol{\sigma}}^{C}_{p} \ . \tag{A.20}$$

Here, the LB-states $\{\hat{\bar{\boldsymbol{\sigma}}}^{BC}_{zpzr}\}$ are shared between networks B and C, while the LB-states $\bar{\boldsymbol{\sigma}}^{B}_{r}$ and $\bar{\boldsymbol{\sigma}}^{B}_{zp}$, that map to load dipoles $\sqrt{2}\hat{\boldsymbol{f}}_r$ and $\sqrt{2}\hat{\boldsymbol{f}}_p$ in network B, are replaced by their commensurate counterparts $\bar{\boldsymbol{\sigma}}^{C}_{zr}$ and $\bar{\boldsymbol{\sigma}}^{C}_{p}$ in network C, consistent with Appendix A.4. Using Eqs. (A.19-A.20) and Eqs. (A.8-A.13), the stress response difference between the two structures then reduces to the following equation:

$$\begin{aligned}
\Delta\boldsymbol{\sigma} &= \boldsymbol{\sigma}^{C} - \boldsymbol{\sigma}^{B} \\
&= \hat{\bar{\boldsymbol{\tau}}}^{B}_{r} \left[C_r \left(\frac{-1 + (\hat{\boldsymbol{r}} \cdot \hat{\bar{\boldsymbol{\tau}}}^{B}_{r})^2}{\hat{\boldsymbol{r}} \cdot \hat{\bar{\boldsymbol{\tau}}}^{B}_{r}} \right) + C_p \left(\frac{-\hat{\bar{\boldsymbol{\tau}}}^{B}_{r} \cdot \hat{\bar{\boldsymbol{\tau}}}^{C}_{p}}{\hat{\boldsymbol{p}} \cdot \hat{\bar{\boldsymbol{\tau}}}^{C}_{p}} \right) \right] \\
&+ \hat{\bar{\boldsymbol{\tau}}}^{C}_{p} \left[C_p \left(\frac{1 - (\hat{\boldsymbol{p}} \cdot \hat{\bar{\boldsymbol{\tau}}}^{C}_{p})^2}{\hat{\boldsymbol{p}} \cdot \hat{\bar{\boldsymbol{\tau}}}^{C}_{p}} \right) + C_r \left(\frac{\hat{\bar{\boldsymbol{\tau}}}^{B}_{r} \cdot \hat{\bar{\boldsymbol{\tau}}}^{C}_{p}}{\hat{\boldsymbol{r}} \cdot \hat{\bar{\boldsymbol{\tau}}}^{B}_{r}} \right) \right] \\
&\in \mathrm{Sp}(\hat{\bar{\boldsymbol{\tau}}}^{B}_{r}, \hat{\bar{\boldsymbol{\tau}}}^{C}_{p}).
\end{aligned} \tag{A.21}$$

Once again, the two networks' stress response difference is contained in the space spanned by their two mutually exclusive SS-states, $\hat{\bar{\boldsymbol{\tau}}}^{B}_{r}$ and $\hat{\bar{\boldsymbol{\tau}}}^{C}_{p}$. Note that the stress response difference of Eq. (A.18) (process I) is a special case of the general expression in Eq. (A.21)

for process II.

Consider finally the two compatible networks A and A', related via process III. With the same procedure as for processes I and II, we can write:

$$\boldsymbol{\sigma}^{A} = \sum_{i=1}^{N_b-2H-1} \left(C_i \hat{\bar{\boldsymbol{\sigma}}}^{A}_{zr,i} \right) + C_r \hat{\boldsymbol{r}} \ , \tag{A.22}$$

while the stress response of network C is given by:

$$\boldsymbol{\sigma}^{A'} = \sum_{i=1}^{N_b-2H-1} \left(C_i \hat{\bar{\boldsymbol{\sigma}}}^{A}_{zr,i} \right) + C_p \hat{\boldsymbol{p}} \tag{A.23}$$

By definition, under a load that is supported in both networks, the coefficients C_r and C_p must be zero (see Appendix A.4); and hence, there is no stress response difference between the two structures A and A' under identical, supported loads. Again, the stress response difference for process III is a special case of Eq. (A.21) for process II.

In conclusion: the stress response difference between two networks (related by a single supertriangle rotation) under identical, supported loading is contained in the span of the structures' mutually exclusive SS-states. There may be zero, one, or two such states, corresponding to processes III, I, and II respectively. The precise magnitude of the stress response difference can be found using Eqs. (A.18) (process I) and (A.21) (process II); the stress response difference for process III is trivially zero.

A.6. BoPET film properties

To create multistable groovy sheets, their base material must be stiff under gravity; deformable with minimal permanent damage; and readily formable into a grooved geometry (section 5.2). Here, we discuss to what extent polymer film meets these criteria.

PET is a thermoplastic polymer resin in the polyester family[169], whose molecular chain contains ester functional groups. BoPET film is typically formed by extruding molten, amorphous resin in two orthogonal directions, and then partially crystallizing the extruded film by heating it above the glass transition temperature under tension[169]. BoPET film is widely used and produced; we use 'Mylar-A' films produced by Dupont Teijin[150]. The mechanical properties of PET film are consistent under a wide range of environmental conditions, and it is therefore used for applications that range from insulation to food packaging. Here, we use the consistency of commercially produced BoPET film to ensure that our experimental findings show a minimal dependence on material variations.

To confirm the reported[150] Young's modulus and yield point at room temperature of Mylar-A BoPET, we perform a series of tensile tests on the material following ASTM-D882[170]. These tensile tests produce stress-strain curves in the material's elastic regime (governed by the Young's modulus) and the plastic regime (determined by the yield point). A schematic of the experimental setup used is shown in Fig. A.5a. Mylar strips of width $W = 20 \pm 1$ mm, total length 150 ± 1 mm, and thickness $t = 23$ µm are mounted manually in clamps connected to an Instron 3360 model universal testing machine (UMT) outfitted with an Instron 2530 series static load cell with a capacity of 100 N[171,172]. The strip's length from clamp to clamp is $L = 100 \pm 1$ mm. The initial configuration is chosen such that the sample is slack in the testing machine, exerting only a gravitational force on the load cell. The UMT's translation stage extends the strip back and forth three times over a range of 1.5 mm at a typical rate of 0.1 mm/s. The translation stage's position and the force exerted on the load cell by the extended sample are recorded at a typical frequency of 5 Hz. Typical extensions u and forces $\langle F \rangle$, averaged over the extension cycles, are shown in Fig. A.5b). Force and extension are converted to engineering stress and strain, σ and ϵ, via:

$$\sigma = \frac{F - F_0}{Wt} \tag{A.24}$$

$$\epsilon = \frac{u - u_0}{L} \ , \tag{A.25}$$

where F_0 and u_0 are the estimates force and extension at the onset of sample stretching. We fit the relation between stress and strain with a Hookean model, $\sigma = E\epsilon$, over a strain range of nearly 0.01 (Fig. A.5c) to obtain an estimate of the Young's modulus E (Fig. A.5d). We estimate the yield point as the stress and strain σ_y and ϵ_y at which the curve deviates significantly from its initial linear trend, obtained from fracture tests on three distinct samples at cycle speeds of 0.1 mm/s (Fig. A.5e-f).

Notably, for large strain rates and sudden extension reversals, the recorded force curves exhibits unusual behaviour. The area under the force-displacement curve measures the energy dissipated during a test cycle. Normally, this area has a positive magnitude, corresponding to hysteretic energy loss: the recorded force under extension is larger than the force under compression. However, at large strain rates, this behaviour reverses due

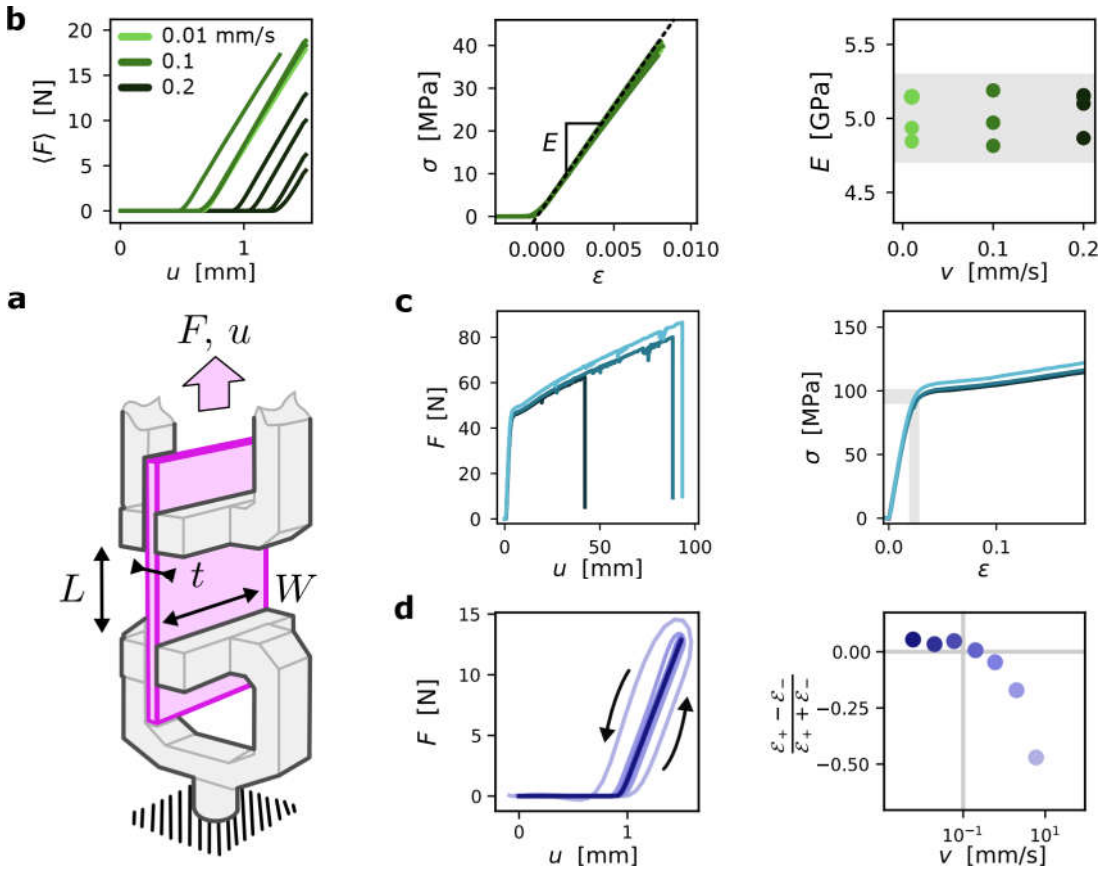

Fig. A.5.: Measuring material properties. **a**, A thin sheet of width $W = 20$ mm and thickness $t = 23$ µm (pink) is fastened between two clamps (grey) to obtain a gauge length $L = 100$ mm. The clamps are mounted in an Instron UTM. Displacement u of the upper clamp produces a force F, measured by a load cell mounted in the UTM. Forces and displacements are converted to engineering stress and strain (main text). **b**, Left to right: typical curves of force $\langle F \rangle$ versus displacement u averaged over three test cycles at variable extension speed v (legend). The corresponding engineering stress and strain σ and ϵ are linearly related via Young's modulus E. The fitted Young's modulus and standard error (grey area, main text) show no significant dependence on speed. **c**, Force-displacement curves until fracture for three samples at speed $v = 0.1$ mm/s (left). In the corresponding stress-strain curves (right), the material's yield point (grey area) is found where the curves deviate from linear behaviour. **d**, Left: high-speed tests produce unphysical results. The extensile force is smaller than the contractile force (arrows; light blue curve) rather than the reverse (normal hysteresis). Right: The normalized work performed by the setup (main text) is measured as a function of test speed. Negative values above 0.2 mm/s are unphysical.

to inertia of the static load cell's response: the compressive force is larger than the extensile force (Fig. A.5g) indicating a testing issue unrelated to the sample's properties. To quantify this behaviour, we compare the energy input and output $\mathcal{E}_+$ and $\mathcal{E}_-$ (that is, the area under the force-displacement curve during extension and retraction) using a normalized metric $\frac{\mathcal{E}_+ - \mathcal{E}_-}{\mathcal{E}_+ + \mathcal{E}_-}$. Fig. A.5h shows that this measure is negative and unphysical at cycle speeds over 0.2 mm/s positive. To ensure the measured material properties are not affected by this issue, we choose a typical cycle speed of 0.1 mm/s.

The standard error on the Young's modulus due to errors in length measurements is estimated at (assuming uncorrelated errors and insignificant errors in force, thickness,

and extension measurements):

$$\Delta E \approx \sqrt{(\frac{\Delta W}{W})^2 + (\frac{\Delta L}{L})^2 + (\frac{\Delta u_0}{u - u_0})^2} E \approx 0.06E \approx 0.3 \text{ GPa} , \tag{A.26}$$

where ΔW and ΔL are estimated at 1 mm and Δu_0 at 0.1 mm.

The resulting experimental estimates of the Young's modulus and yield stress are $E = 5 \pm 0.3$ GPa, averaged over 7 distinct samples; all measurements fall within the error margin. Additionally, we find a yield stress and strain $\sigma_y = 96 \pm 5$ MPa and $\epsilon_y = 0.025 \pm 0.007$, estimated from fracture tests on 3 samples. Our findings are consistent with the reported material properties.

A.7. Spring-back, yielding, and groove design

We would like to understand the effect that our thermoforming methods have on thin BoPET films (section 5.2). Here, we relate the post-forming shape of groovy sheets to the geometry imposed during thermoforming, via a simple model for plastic deformation[173]. In this model, applying a moment to a flat sheet produces an internal stress and strain field. If the stress exceeds a certain limit, the sheet deforms plastically. When the external moment is removed, a residual strain remains and sets the final shape of the sheet. Below, we quantify the difference between the imposed and final groove shape in terms of spring-back.

We assume a bilinear constitutive model for the material's stress-strain curve at room temperature (Fig. A.6a). The model is given by the following relation between stress σ and strain ϵ:

$$\sigma = \begin{cases} E\epsilon & : \epsilon \leq \epsilon_y \\ E\epsilon_y & : \epsilon > \epsilon_y \end{cases} \tag{A.27}$$

This constitutive model has an elastic regime, set by the Young's modulus E (the slope of the stress-strain curve in the elastic regime) and a plastic regime, set by the yield point (at a stress $\sigma_y = E\epsilon_y$ and strain ϵ_y, beyond which the stress is independent of the applied strain).

With the above model, we now make a prediction for the residual stresses, strains, and final shape of a thin sheet section of length $R\theta$ and width W (Fig. A.6b) that is forced to curve into a radius R over a subtended angle θ by applying a bending moment M (Fig. A.6c). The bending moment leads to a through-thickness strain ϵ. Since the sheet's thickness is small compared to other relevant length scales, there are no strains in any other directions. We calculate ϵ along the local coordinate ζ, which runs from the sheet's neutral axis along the surface normal. All (virtual) lines in the sheet parallel to the neutral axis undergo a length change from $R\theta$ to $(R+\zeta)\theta$. Thus, the engineering strain through the sheet's thickness is given by

$$\epsilon(\zeta) = \frac{(R+\zeta)\theta - R\theta}{R\theta} = \frac{\zeta}{R} \ . \tag{A.28}$$

When the sheet is curved strongly, the yield point is exceeded at the outer layers of the sheet, at a yield thickness $\zeta > \zeta^* = R\epsilon_y$. The corresponding engineering stress profile, $\sigma(\zeta)$, is then

$$\sigma(\zeta) = \begin{cases} E\frac{\zeta}{R} & : \zeta \leq \zeta^* \\ E\epsilon_y & : \zeta > \zeta^* \end{cases} \tag{A.29}$$

The moment M that must be exerted on the sheet to obtain the curvature R is then given by:

$$M = W\int_{t/2}^{t/2} \sigma(\zeta)\zeta \mathrm{d}\zeta = \frac{WE\epsilon_y}{12}\left(3t^2 - 4{\zeta^*}^2\right) \tag{A.30}$$

When this external moment is removed, the sheet relaxes into a new configuration, with a residual strain $\epsilon'(\zeta)$ and stress $\sigma'(\zeta)$ that respect moment balance $M' = 0$ and the

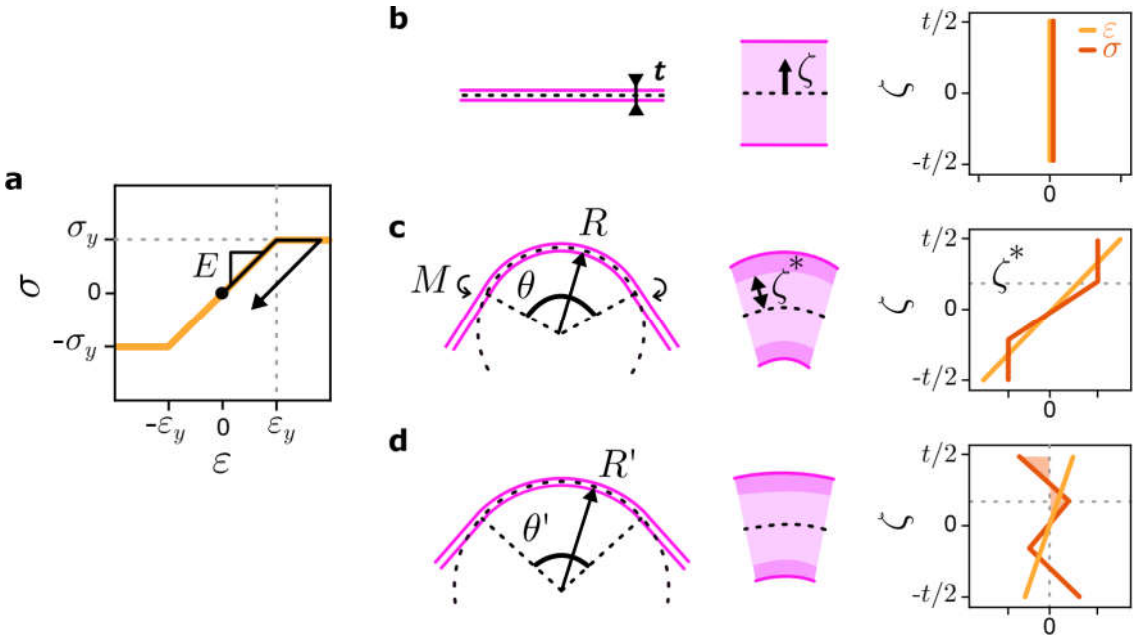

Fig. A.6.: Modelling plastic deformations of a thin film. **a**, A stress-strain relation $\sigma(\epsilon)$ (yellow line) to model plastic deformations. Small strains induce reversible stress proportional to the Young's modulus E. Above yield stress σ_y, achieved at strain ϵ_y, deformations are irreversible and the stress is constant. The stress-strain trajectory (black line) of a material under (partially) plastic deformation is illustrated. **b**, A thin flat sheet of thickness t (left) with zero initial stress or strain along the sheet's normal direction ζ, measured from the sheet's centre (middle, right). **c**, Bending the sheet to a curvature R over a length θR by applying a moment M (left) induces plastic deformations up to a thickness ζ^* (middle), above which the yield stress is exceeded (right). **d**, Removing the moment (left, middle) relaxes the sheet to a curvature R' over length $R'\theta'$. The relaxed curvature is due to residual stresses and strains in the material (right).

constitutive equations, $\sigma'(\zeta) = \sigma(\zeta) - E(\epsilon - \epsilon')$ (Fig. A.6d). Thus, we find

$$M' = W \int_{t/2}^{t/2} \sigma'(\zeta)\zeta \mathrm{d}\zeta = \frac{EW}{12}\epsilon_y \left(3t^2 - 4\zeta^{*2}\right) + \frac{EW}{12}t^3(\frac{1}{R'} - \frac{1}{R}) = 0 \ , \tag{A.31}$$

from which we obtain an expression for the spring-back in terms of the difference between imposed and relaxed curvatures $\kappa' = \frac{1}{R'}$ and $\kappa - \frac{1}{R}$:

$$\kappa' - \kappa = \frac{\epsilon_y}{t}\left(4(\frac{R\epsilon_y}{t})^2 - 3\right) \ . \tag{A.32}$$

From this equation, we see that the relaxed curvature κ' is (of course) always smaller than the imposed curvature κ: there is always some spring-back that flattens the sheet out after deformation. Note that the amount of spring-back is maximal when the yield thickness lies outside the sheet, $\zeta^* > t/2$, in which case $\kappa' - \kappa = -\kappa$: the sheet does not deform plastically. Conversely, when the yield thickness is much smaller than the sheet thickness, the spring-back decreases proportionally: $\kappa' - \kappa = -3\epsilon_y/t$.

As an aside, note that the opening angle θ and radius of curvature R before and after forming are related, since the neutral axis' length remains constant:

$$R\theta = R'\theta' \ . \tag{A.33}$$

As a back-of-the-envelope check, observations show that a visible permanent deformation is left in thin sheets of thicknesses $15, 23, 50$, and 100 µm at the following radii of curvature: $0.2, 0.5, 1$, and 2 mm. At these radii, the plasticity-free region inside the sheet has a thickness of $2\epsilon_y R$, or approximately (assuming $\epsilon_y = 0.02$) $8, 20, 40$, and 80 µm respectively. These qualitative results support the validity of our simple model.

We use the model presented above to estimate which groove geometries do not give rise to significant plastic deformation after the initial forming stage. During typical experiments, the material's yield stress may not be exceeded; in practise, this means that the groove's radius of curvature R must be much larger than the sheet's thickness t. Here, we estimate a lower bound for the ratio between R and t, above which we expect minimal yielding of the sheets during our experiments.

Consider a sheet section where an applied moment produces a positive radius of curvature R: this is the initial forming stage. A subsequent opposite moment changes the radius of curvature to zero, flattening the sheet, which models subsequent probing of the sheet. We now estimate the maximal initial radius of curvature that may be flattened without inducing extra plasticity. The initially applied strain and stress profiles are, as before,

$$\epsilon(\zeta) = \frac{\zeta}{R} \tag{A.34}$$

$$\sigma(\zeta) = \begin{cases} E\frac{\zeta}{R} & : \zeta \leq \zeta^* \\ \sigma_y & : \zeta > \zeta^* \end{cases} \ , \tag{A.35}$$

where $\zeta^* = R\sigma_y/E$ is the groove's yield thickness. Applying a flattening strain $\Delta\epsilon = -\frac{\zeta}{R}$ will lead to no yielding at the sheet surface under the following condition:

$$\frac{R}{t} > \frac{E}{4\sigma_y} \ , \tag{A.36}$$

that is, the ratio between the initial radius of curvature and sheet thickness must be larger than a quarter of the ratio between Young's modulus and yield stress. Equivalently, the yield thickness ζ^* must be larger than a quarter of the sheet thickness t.

Note that the above result is derived from a model with no temperature increase during the initial plastic deformation. If such a temperature increase is incorporated, the corresponding stress relaxation inside the sheet allows for a stronger initial curvature without plastic deformations under flattening. Therefore, our result above forms a sensible lower limit for the ratio between the forming radius and sheet thickness.

Mylar-A BoPET has a reported Young's modulus $E = 4$ GPa and a yield stress 71 MPa. Thus, we find a safe shape limit as

$$\frac{R}{t} \approx 14 \ .$$

We use BoPET sheets with thicknesses between 23 and 100 µm. The corresponding minimal radius of forming curvature to prevent plastic deformations under flattening then lies between 0.3 and 1.4 mm. Thus, we aim for groove shapes with radii of curvature above this size range.

A.8. Elasticity of groovy sheets: accordion model

We present the mathematical analysis of the accordion model discussed in section 5.4.4 here. The accordion mimics the in-plane stretching response of a groovy sheet. The accordion consists of $2N$ bars of length s^0 and stiffness k_t connected by torsional springs of stiffness k_s and rest angle ϕ^0, forming a structure with N grooves. Extension by a force F produces an elongation u; the system's Lagrangian $\mathcal{L}$ is given by

$$\mathcal{L} = -2N\frac{1}{2}k_t(\phi-\phi_0)^2 - 2N\frac{1}{2}k_s(s-s^0)^2 + F\left(u - 2N(s\cos\frac{\phi}{2} - s^0\cos\frac{\phi^0}{2})\right) , \tag{A.37}$$

where the first term on the right hand side corresponds to opening of the grooves, the second to stretching of the bars, and the third to a length constraint enforced by the Lagrange multiplier F. Minimization of the Lagrangian with respect to the fold angle ϕ, bar length s, and force F produce a system of coupled governing equations,

$$k_s(s-s^0) = -F\cos\frac{\phi}{2} \tag{A.38}$$

$$k_t(\phi-\phi^0) = F\frac{s}{2}\sin\frac{\phi}{2} \tag{A.39}$$

$$u_x = 2N(s\cos\frac{\phi}{2} - s^0\cos\frac{\phi^0}{2}) \ . \tag{A.40}$$

There are analytic solutions for F in terms of the extension u only in the limits of small or large displacements, as we show now.

We first consider where a crossover from small to large values of the extension takes place, by considering when the bar length changes significantly so that $\Delta s = s - s^0$ becomes large compared to s^0. With the equilibrium equations above, we express the bar length as a function of fold angle:

$$s = \frac{s^0}{2}\left(1 + \sqrt{1 - 8\frac{k_t}{(s^0)^2k_s}\frac{\phi-\phi^0}{\tan\frac{\phi}{2}}}\right) \tag{A.41}$$

$$\frac{\Delta s}{s^0} = \frac{1}{2}\left(\sqrt{1 - 8\frac{k_t}{(s^0)^2k_s}\frac{\phi-\phi^0}{\tan\frac{\phi}{2}}} - 1\right) \ . \tag{A.42}$$

Evidently, bar stretching is important if the (positive) quantity $-8\frac{k_t}{l_0^2k_s}\frac{\phi-\phi^0}{\tan\frac{\phi}{2}}$ becomes significant compared to unity. If we consider a value of $8C$, where C is some small constant below e.g. 0.01, we find a crossover inequality:

$$\frac{\phi-\phi^0}{\tan\frac{\phi}{2}} > C\frac{(s^0)^2k_s}{k_t} \ . \tag{A.43}$$

This transcendental inequality can be evaluated numerically for an accordion model of fixed stiffness and geometry. From numerical investigations, we find that the quantities ϕ and $\frac{(s^0)^2k_s}{k_t}$ are typically of the same order of magnitude around the crossover region. Assuming that realistic estimates for the bars and hinges' stiffness scale with the real sheet's thickness $t \lesssim \mathcal{O}\left(10^{-4}\right)$ m to first and third order respectively, and that the bar

length lies around $s^0 \gtrsim \mathcal{O}\left(10^{-3}\right)$ m, we find $\frac{(s^0)^2 k_s}{k_t} \lesssim \mathcal{O}\left(10^{-2}\right)$. This in turn implies that the accordion must flatten out almost completely, $\phi \lesssim \mathcal{O}\left(10^{-2}\right)$, for bar stretching to become significant.

Secondly, we consider the below-crossover regime, where the accordion has not flattened out and bar stretching is not significant. In that case, from Eq. A.39, we find

$$\lim_{s \to s^0} u = 2Ns^0(\cos\frac{\phi}{2} - \cos\frac{\phi^0}{2}) \tag{A.44}$$

$$\lim_{s \to s^0} F = 2\kappa \frac{\phi - \phi^0}{s^0 \sin\frac{\phi}{2}} \approx -\frac{8Nk_t}{(2Ns^0 sin\frac{\phi^0}{2})^2} u + \mathcal{O}\left(u^2\right) \tag{A.45}$$

which corresponds to a rigid-bar model with infinitely large stretching stiffness. Note here that the relation between force and displacement $F(u)$ is linear for small values of u only.

Thirdly, we study the above-crossover regime, where the accordion is fully flattened and bar stretching dominates the response. With the governing equations A.38- A.40, we find

$$\lim_{\phi \to 0} u = 2N(s - s^0 \cos\frac{\phi^0}{2}) \tag{A.46}$$

$$\lim_{\phi \to 0} F = \lim_{\phi \to 0} k_s(s - s^0)/\cos\frac{\phi}{2} = k_s\left(\frac{u}{2N} - s^0(1 - \cos\frac{\phi^0}{2})\right) \tag{A.47}$$

As expected, the force increase in this regime is purely due to bar stretching.

In short, when the accordion is stretched, fold opening dominates at first. If the stiffness ratio $\frac{(s^0)^2 k_s}{k_t}$ is small, the model's response crosses over to bar stretching after the accordion is almost fully flattened.

A.9. 3D numerical sheet model

We construct a simple numerical model that mimics the behaviour of groovy sheets.

A simulated groovy sheet is shown in Fig. A.7a. The structure consists of squares of Hookean springs with unit length $l = 1$ and unit stiffness $k_s = 1$, cross-braced by diagonal springs (length $\sqrt{2}l$ and stiffness k_{sd}). The springs are connected at their corners by nodes with a torsional stiffness k_t. The square cells are arranged in an accordion-like pattern at a fold angle ϕ^0 to copy the geometry of a real groovy sheet.

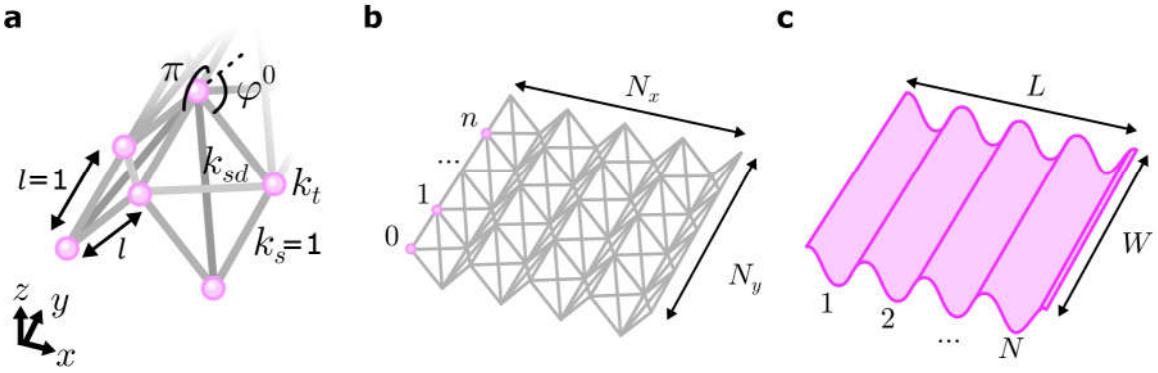

Fig. A.7.: Computational model of a groovy sheet. a, Zoom-in of the model: a square lattice (grey bars) of Hookean edge springs (length l, stiffness k_s) cross-braced by diagonal springs (length $\sqrt{2}l$, stiffness k_{sd}) and connected by nodes (pink circles) with torsional hinges (stiffness k_t, and resting angle ϕ^0 along $\hat{\boldsymbol{x}}$ and π along $\hat{\boldsymbol{y}}$). **b,** A model sheet of N_x by N_y nodes; indices n are indicated to show node numbering convention. **c,** The discrete structure aims to model to a groovy sheet with N grooves, width W, and length L.

A.9.1. Parameters

In order to mimic a groovy sheet's elastic properties, the model is assigned the following parameters. First, we rescale all lengths and stiffnesses by the square cell size and the edge spring stiffness, $l = 1$ and $k_s = 1$. Lengths are thus measured in terms of the cell size l, and energies are measured in units $k_s l^2$. One unit of energy then corresponds to the work needed to stretch an edge spring to twice its length. To ensure an isotropic in-plane response, the diagonal springs must have a stiffness $0.5k_s$. However, this value overestimates the bending energy of the facets, and we choose a slightly lower value of $k_{\mathrm{sd}} = 0.1k_s$ instead. In addition, we expect the facet bending The torsional stiffness is set to $k_t = 1 \cdot 10^{-4}$, which is the same order of magnitude as the ratio between torsional and stretching stiffness in a real sheet (see section 5.4.5). Finally, the fold angle is set to $\phi^0 = 2\mathrm{rad}$, which yields an amplitude-to-groove size ratio $A/s_\lambda \approx 0.3$, similar to that of real grooves (section 5.2.2).

A.9.2. Algorithm

The simulated sheet's mechanics are probed as follows. While all springs in the structure are initially at rest at time $t = 0$, with the nodes at position vector $\boldsymbol{Q}^{t=0}$, the springs

can be deformed by displacing selected nodes to new positions $\boldsymbol{Q}^{t=1}$. To find the sheet's final shape under the applied displacement, it is slowly relaxed to a mechanical equilibrium (that is, a minimal energy $\mathcal{E}(\boldsymbol{Q})$) via a two-step gradient descent algorithm. First, the restoring force $\nabla_Q \mathcal{E}$ on each node is calculated from the deformed sheet geometry. Second, each node is displaced in the direction of its restoring force, modified by a multiplicative *gradient descent parameter* α. These two steps are iterated: the restoring force is calculated and corresponding node displacements are applied as follows:

$$\boldsymbol{Q}^{t+1} = \boldsymbol{Q}^t - \alpha \nabla_Q \mathcal{E}(\boldsymbol{Q}^t) \ , \tag{A.48}$$

until either the system's geometrical change $|\Delta \boldsymbol{Q}|$ becomes insignificant compared to machine precision, or until a computationally reasonable maximal number of iterations (here, we choose $t_{\max} = 10^6$) is reached. We choose a gradient descent parameter $\alpha = 0.25$, maximal loops $t_{\max} = 10^6$, and cutoff geometric change $|\Delta \boldsymbol{Q}| = 10^{-15}$. After this optimization procedure, the sheet's equilibrium configuration under the imposed constraints is reached with good accuracy: the geometric change shows a steady, logarithmic decrease below $|\Delta \boldsymbol{Q}| < 10^{-6}$ (a reasonable size compared to the length and stiffness scales used) by the end of all simulations presented here.

A.9.3. Energy and forces

We briefly summarize the mathematical implementation of the sheet model and its gradient descent algorithm below. The model's configuration is fully described by the node positions $q_{i,n}$, collected in the position vector

$$\boldsymbol{Q} = (q_{x,0}, q_{y,0}, q_{z,0}, ..., q_{x,N_{\text{tot}}-1}, q_{y,N_{\text{tot}}-1}, q_{z,N_{\text{tot}}-1}) \ , \tag{A.49}$$

where n indexes the network's N_{tot} nodes and i indexes the coordinates x,y and z. A sheet with N grooves, width W and wavelength λ is thus modelled by a network of $N_x = 2N + 1$ by $N_y = \lceil W/\lambda \rceil$ nodes, totalling $N_{\text{tot}} = N_x N_y$. We adopt a standard numbering convention using indices $n_x \in [0, N_x - 1], n_y \in [0, N_y - 1]$, so that $n = n_x N_x + n_y$. With this convention, the initial position $\boldsymbol{q}_n$ of node n is given by

$$\boldsymbol{q}_n = l(n_x \cos\frac{\phi}{2}, n_y, (-1)^{n_x+1}\frac{1}{2}\sin\frac{\phi}{2}) \ . \tag{A.50}$$

Each node is connected via harmonic springs to *i)* nearest neighbours (NN) by a Hookean edge spring of length l and stiffness k_t; *ii)* next-nearest neighbours (NNN) by a diagonal Hookean spring of length $\sqrt{2}l$ and stiffness k_{td}; and *iii)* next-next-nearest neighbour (NNNN) pairs by a torsional spring of stiffness k_t with rest angle $\theta = \pi - \phi$ along $\hat{\boldsymbol{x}}$, and with rest angle π along $\hat{\boldsymbol{y}}$. Deformation of these springs costs elastic energy, which is calculated from the node positions $\boldsymbol{Q}$ as follows:

$$\mathcal{E}(Q) = \frac{1}{2}\sum_{\text{NN}} k_s (l'_{rs} - l_{rs})^2 + \frac{1}{2}\sum_{\text{NNN}} k_{sd}(l'_{rs} - l_{rs})^2 \tag{A.51}$$

$$+\frac{1}{2}\sum_{\text{NNNN}} k_t(\theta'_{rst} - \theta_{rst})^2 \ , \tag{A.52}$$

where superscripts signify deformed spring lengths and angles. Spring lengths and angles are calculated via

$$l_{rs} = |\boldsymbol{q}_r - \boldsymbol{q}_s| \tag{A.53}$$

$$\theta_{rst} = \arccos\left(\frac{(\boldsymbol{q}_r - \boldsymbol{q}_s)\cdot(\boldsymbol{q}_t - \boldsymbol{q}_s)}{l_{rs}l_{st}}\right) . \tag{A.54}$$

The force experienced by the network nodes, $\nabla_Q \mathcal{E}(Q)$, is calculated by taking the derivative of the total energy $\mathcal{E}(Q)$ with respect to each node's position $\boldsymbol{q}_n$:

$$\begin{aligned}
\frac{\partial \mathcal{E}}{\partial \boldsymbol{q}_n} = &\sum_{n\in \mathrm{NN}} k_s \left(1 - \frac{l_{ns}}{|\boldsymbol{q}_n - \boldsymbol{q}_s|}\right)(\boldsymbol{q}_n - \boldsymbol{q}_s) \\
&+ \sum_{n\in \mathrm{NNN}} k_{sd} \left(1 - \frac{l_{ns}}{|\boldsymbol{q}_n - \boldsymbol{q}_s|}\right)(\boldsymbol{q}_n - \boldsymbol{q}_s) \\
&+ \sum_{\mathrm{NNNN}\ nst} -k_t(\theta'_{nst} - \theta_{nst}) \frac{1}{l'_{ns}} \frac{\mathrm{Rej}(\hat{\boldsymbol{u}}_{st}, \hat{\boldsymbol{u}}_{sn})}{|\mathrm{Rej}(\hat{\boldsymbol{u}}_{st}, \hat{\boldsymbol{u}}_{sn})|} \\
&+ \sum_{\mathrm{NNNN}\ rnt} k_t(\theta'_{rnt} - \theta_{rnt}) \left(\frac{1}{l'_{rn}} \frac{\mathrm{Rej}(\hat{\boldsymbol{u}}_{nt}, \hat{\boldsymbol{u}}_{nr})}{|\mathrm{Rej}(\hat{\boldsymbol{u}}_{nt}, \hat{\boldsymbol{u}}_{nr})|} + \frac{1}{l'_{tn}} \frac{\mathrm{Rej}(\hat{\boldsymbol{u}}_{nr}, \hat{\boldsymbol{u}}_{nt})}{|\mathrm{Rej}(\hat{\boldsymbol{u}}_{nr}, \hat{\boldsymbol{u}}_{nt})|}\right) .
\end{aligned}$$

Here, $\mathrm{Rej}(\boldsymbol{u}, \boldsymbol{v})$ indicates the vector rejection $\boldsymbol{u} - (\boldsymbol{u}\cdot\hat{\boldsymbol{v}})\hat{\boldsymbol{v}}$ of $\boldsymbol{u}$ on $\boldsymbol{v}$. Indices (r, s, t) refer to an ordered triad of next-next-nearest neighbour nodes at positions $\boldsymbol{q}_r$,$\boldsymbol{q}_s$ and $\boldsymbol{q}_t$ connected by a torsional spring with rest angle θ_{rst}. The line connecting centre node s to node r is described by $\hat{\boldsymbol{u}}_{sr} = \frac{\boldsymbol{q}_s - \boldsymbol{q}_r}{l_{rs}}$. Physically, forcible opening of the triad's rest angle results in restoring forces that bring nodes r and t away from (and node s toward) the triad's centre of mass, which produces in a fold-closing motion during gradient descent optimization. To account for orientation during the angle calculation, we check the orientation of the outer product of $\hat{\boldsymbol{u}}_{st}$ and $\hat{\boldsymbol{u}}_{sr}$ with respect to the locations of nearest neighbour nodes; a switch in alignment of this vector compared to the configuration at rest means that the complement angle to the numerical value $\arccos\cos\theta_{rst}$ must be used instead. The energy and restoring force are calculated at each time step by querying all nodes, which results in an algorithm with complexity $\mathcal{O}(N_{\mathrm{tot}})$.

A.10. Defect energetics in a 3D numerical sheet model

In section 5.6.2, Fig. 5.34, the elastic energy of an equal- and opposite-parity defect pair was calculated with the computational model outlined in section 5.4.5. Reference curves were shown that correspond to the energy needed to create the pair's two defects individually. The reference curves were obtained by calculating the energy of isolated defects, as follows.

Fig. A.8a shows the network model consisting of square cells of Hookean springs (stiffness $k_s = 1$ for cell edges and $0.1k_s$ for diagonal braces), connected by torsional springs (stiffness $k_t = 1 \cdot 10^{-4}$). The model is discrete: the smallest length scale is the cell size, $l = 1$. Fig. A.8b shows a positive (negative) defect, created at a distance w from the sheet centre, at energy cost $\mathcal{E}_+$ ($\mathcal{E}_-$). The defect's energy varies with its position, as shown in Fig. A.8c.

Defects can only be made along a groove at integer multiples of l. To ensure defect *pairs* are as symmetrically spaced as possible at a mutual distance d, the first defect is created at $w = \lceil \frac{d}{2} \rceil$; the second at $w = \lfloor \frac{d}{2} \rfloor$, where brackets $\lceil\ \rceil$ and $\lfloor\ \rfloor$ refer to rounding to the nearest larger and smaller integer, respectively. Thus, the pair energy $\mathcal{E}_{++}(d)$ should be compared to the sum of individual energies

$$\sum \mathcal{E}_+(d) = \mathcal{E}_+(\lceil \frac{d}{2} \rceil) + \mathcal{E}_+(\lfloor \frac{d}{2} \rfloor) \ , \tag{A.55}$$

and similarly, pair energy $\mathcal{E}_{+-}(d)$ must be contrasted to the sum of individual energies

$$\sum \mathcal{E}_\pm(d) = \mathcal{E}_-(\lceil \frac{d}{2} \rceil) + \mathcal{E}_+(\lfloor \frac{d}{2} \rfloor) \ . \tag{A.56}$$

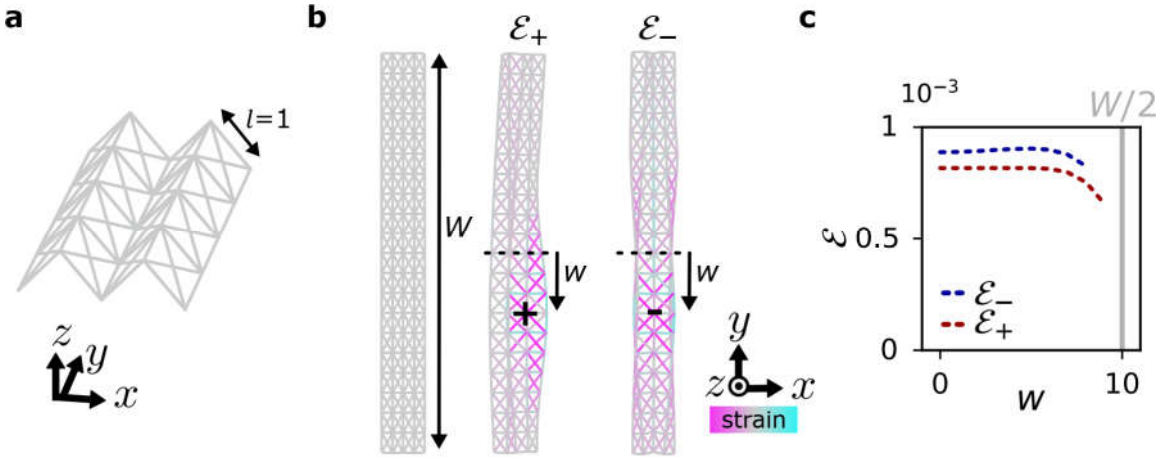

Fig. A.8.: Modelling defect energy. **a,** Zoom-in of network model consisting of Hookean springs connected by torsional hinges. Lengths are measured in terms of cell size $l = 1$. **b,** Model sheet with $N = 2$ grooves and width $W = 20$ (left). A defect is made at distance w from the sheet centre, either in a mountain fold at energy cost $\mathcal{E}_+$ (middle), or in a valley fold at energy cost $\mathcal{E}_-$ (right). Spring strain indicated for clarity (colour bar). **c,** Energies $\mathcal{E}_+$ ($\mathcal{E}_-$) as a function of w.

A.11. Calculating surface curvature

We briefly review how we compute the curvature of a groovy sheet from its three-dimensional profile, obtained via the 3D-scanning method described in section 5.3.2.

3D-scanned height profiles z on a square grid in the x, y-plane form our starting point. The height profile's discrete derivatives, $\frac{\partial z}{\partial x}$ and $\frac{\partial z}{\partial y}$, must be calculated to obtain surface curvatures. Making use of the fact that our measurements produce height profiles with a regular grid spacing, we use the following formula to calculate a five-point discrete derivative at each grid site (x_i, y_i)[174]:

$$\frac{\partial z}{\partial x}|_{x_i,y_i} \approx \frac{8(z(x_{i+1}, y_i) - z(x_{i-1}, y_i)) - (z(x_{i+2}, y_i) - z(x_{i-2}, y_i))}{6(x_{i+1} - x_{i-1})} \tag{A.57}$$

Finally, we calculate the mean and Gaussian curvatures K_m and K_g from the discrete derivatives as follows[108]:

$$K_m = \frac{(1 + (\frac{\partial z}{\partial x})^2)\frac{\partial^2 z}{\partial y^2} + (1 + (\frac{\partial z}{\partial y})^2)\frac{\partial^2 z}{\partial x^2} - 2\frac{\partial z}{\partial x}\frac{\partial z}{\partial y}\frac{\partial z}{\partial x \partial y}\frac{\partial z}{\partial y \partial x}}{2(1 + \frac{\partial z}{\partial x}^2 + \frac{\partial z}{\partial y}^2)^{3/2}} \tag{A.58}$$

$$K_g = \frac{\frac{\partial^2 z}{\partial x^2}\frac{\partial^2 z}{\partial y^2} - \frac{\partial z}{\partial x \partial y}\frac{\partial z}{\partial y \partial x}}{(1 + \frac{\partial z}{\partial x}^2 + \frac{\partial z}{\partial y}^2)^2} \tag{A.59}$$

The principal curvatures, K_1 and K_2, can be obtained via:

$$K_1 = K_m - \sqrt{K_m^2 - K_g} \tag{A.60}$$

$$K_2 = K_m + \sqrt{K_m^2 - K_g}\ . \tag{A.61}$$

The principal curvatures are the minimal and maximal values of the local 2D curvature field. As an example, Fig. A.9 shows the principal curvatures of groovy sheets with various defects and defect pairs. The presented data correspond directly to the mean and Gaussian curvatures illustrated in Fig. 5.37.

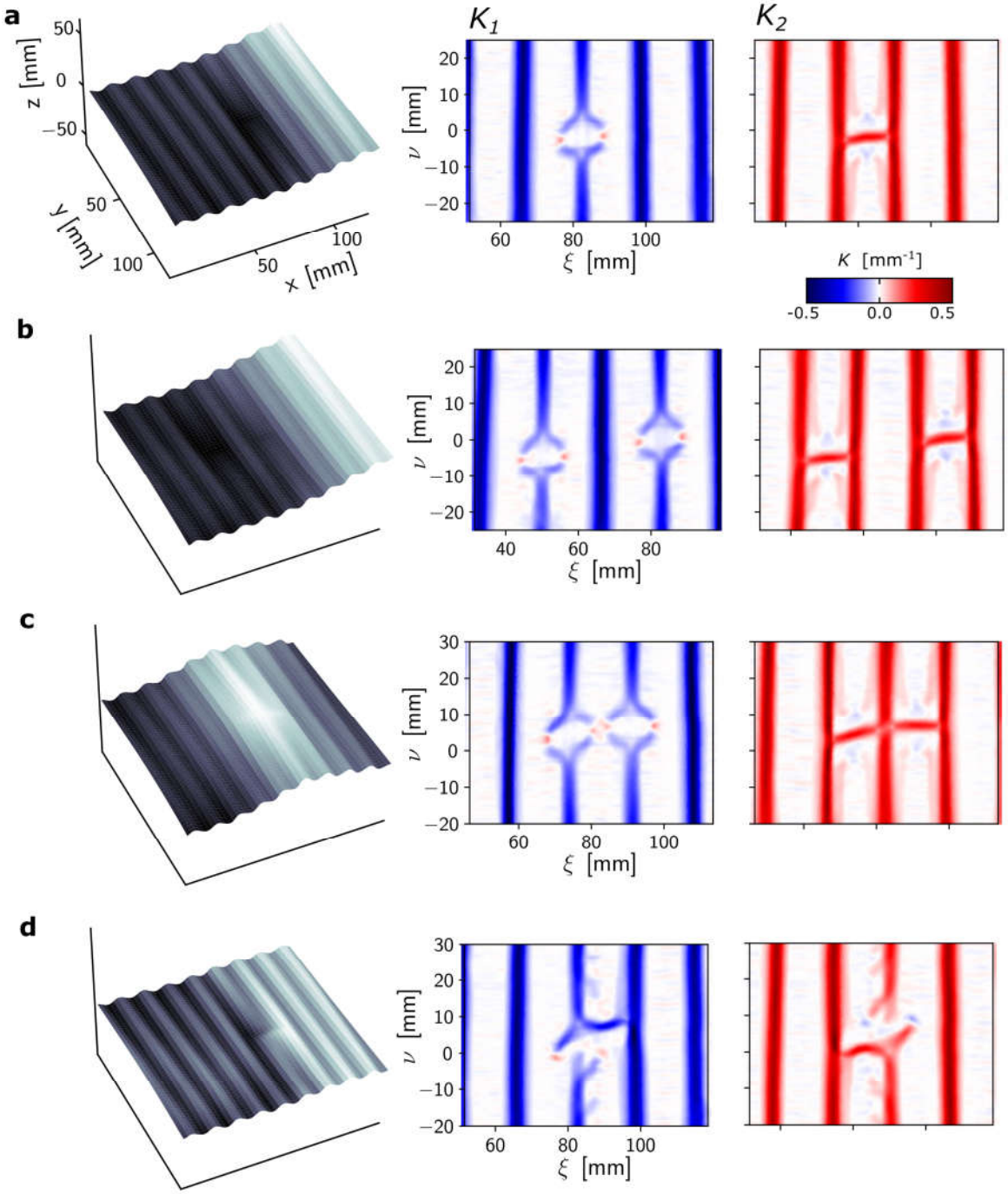

Fig. A.9.: Principal curvatures in the presence of defects. **a,** Principal curvatures K_1 and K_2 (right, colour bar) in a groovy sheet with one defect. The sheet has thickness $75\ \mu\mathrm{m}$, width $W = 13\ \mathrm{cm}$, and $N = 10$ grooves (left; greyscale matches height z) **b,** Curvatures for an adjacent, equal-parity defect pair at a distance of $0\ \mathrm{cm}$ along ν (and two grooves core separation along ξ). **c,** Results for an adjacent equal-parity defect pair at a core separation of one groove. **d,** Adjacent opposite-parity defect pair at half a groove core separation.

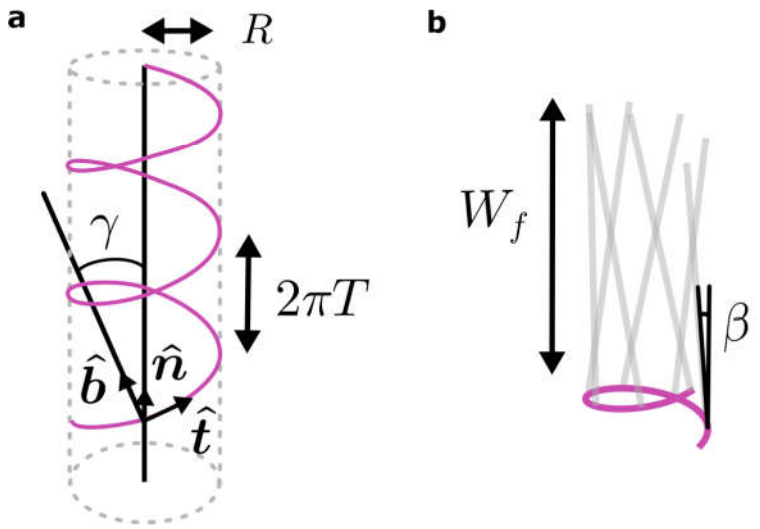

Fig. A.10.: A helix and a corresponding ruled surface. **a,** A helical curve (pink line) with radius R and wavelength $2\pi T$ has local coordinate frame $(\hat{\boldsymbol{t}}, \hat{\boldsymbol{n}}, \hat{\boldsymbol{b}})$. Binormal vector $\hat{\boldsymbol{b}}$ has angle $\gamma = \arctan T/R$ with respect to the cylinder axis. **b,** Ruled surface generated by drawing straight lines (grey lines) of length W_f that point away from the helical curve at a small angle β; local rule direction is given by $\cos\beta\hat{\boldsymbol{b}} + \sin\beta\hat{\boldsymbol{n}}$.

A.12. Elastic model of groovy sheets with a single scar line

Groovy sheets with a single central scar line orthogonal to their grooves roll up. If the scar's distance to the sheet edge, W_f, is large, the sheet undergoes a transition to a twisted shape (see e.g. Fig. 5.40). Here, we construct an energetic model to investigate the origin of this twisting bifurcation. Our findings suggest that this bifurcation arises from an energetic competition between deformations of the scar line and deformations in the rest of the sheet.

Intuitively, the twisting bifurcation takes place to relieve compressive strain between neighbouring grooves. Consider a rolled sheet with a single curved scar line, where grooves point away from the scar line at a small angle. The grooves form a conical cage: they are far apart at the scar line, but converge away from the scar line. At large sheet widths, the grooves must intersect to maintain the rolled sheet shape, indicating that grooves are highly compressed. In order to relieve this compression, the scar line may twist, which allows the grooves to spread (similar to a hyperboloid of one sheet, as seen in wicker chairs). We capture this intuition in a simplified model, as follows.

We assume that rolled sheets can be described as ruled surfaces, as illustrated in Fig. A.10: the scar line forms a generating curve, and grooves are modelled as straight lines that point away from the base curve. We approximate the scar line as a helical base curve $h(t)$ with constant radius R and constant wavelength $2\pi T$, which is described by the parametrization

$$\boldsymbol{h}(t) = (R\cos s, R\sin s, Tt)\ , \tag{A.62}$$

as shown in Fig. A.10a. The base curve has a local coordinate frame (the Serret-Frénet frame), which is given by the tangent, normal, and binormal vectors:

$$\hat{\boldsymbol{t}} = \frac{1}{\sqrt{R^2+T^2}}(-R\sin t, R\cos t, T) \tag{A.63}$$

$$\hat{\boldsymbol{n}} = (-\cos t, -\sin t, 0) \tag{A.64}$$

$$\hat{\boldsymbol{b}} = \frac{1}{\sqrt{R^2+T^2}}(T\sin t, -T\cos t, R)\ . \tag{A.65}$$

The angle between the binormal vector and the cylinder axis is set by $\gamma = \arctan T/R$. The helix' curvature k and torsion g are constants, calculated to be $k = |\frac{\partial t}{\partial s}| = \frac{|R|}{T^2+R^2}$ and $g = \hat{\boldsymbol{b}} \cdot |\frac{\partial n}{\partial s}| = \frac{T}{T^2+R^2}$, where $s = \sqrt{T^2+R^2}t$ is the arc length along the helix. Fig. A.10b illustrates how grooves are modelled as straight lines of length W_f, that point away from the scar line along vectors $\cos\beta\hat{\boldsymbol{b}} + \sin\beta\hat{\boldsymbol{n}}$, where β is a constant, small angle. Thus, the scar line and grooves, via radius R and twist T, and angle β and groove length W_f respectively, set the shape of the modelled sheet; we assume that these shape parameters are constant along the entirety of the sheet.

In order to mimic the elastic properties of a real sheet, we now model the energy costs for deformations of the scar line, and for distortions of the grooves.

We first consider the elasticity of the scar line. We assume that the scar line has a preferred curvature $k^0 = \frac{1}{R^0}$ and torsion $g^0 = 0$. We estimate the resting radius $R^0 \approx \frac{s_\lambda}{2\sin\theta/2} = \mathcal{O}(10\text{ mm})$, based on the experiments illustrated in Fig. 5.40 and the geometric argument shown in Fig. 5.41. Note that we assume here, as before, that grooves are flattened completely at the scar line to their full arc length s_λ. Deviations from the scar's resting curvature and torsion for a scar line section of length s_λ, between two grooves, are then penalized via:

$$\mathcal{E}_k \sim (k-k^0)^2 s_\lambda\ , \tag{A.66}$$

$$\mathcal{E}_g \sim (g-g^0)^2 s_\lambda\ . \tag{A.67}$$

Secondly, we assume that grooves point orthogonally away from the scar line at small preferred folding angle β^0. We estimate $\beta^0 \approx 0.2$ based on experiments (Fig. 5.40). We assume that the folding of grooves around the scar line takes place over a characteristic width comparable to the groove wavelength λ. The energy cost for deviations of the folding angle β over a scar line section of length s_λ is then modelled as

$$\mathcal{E}_\beta \sim \left(\frac{\beta-\beta^0}{\lambda}\right)^2 s_\lambda\ . \tag{A.68}$$

Lastly, we attribute an energy cost to sheet deformations away from the scar line. The sheet prefers to remain flat, its grooves parallel; thus, rolling and splaying (either in- or out-of-plane) of the grooves is penalized. We first consider how much the sheet rolls. Specifically, if the scar line has a finite radius of curvature R, the sheet's local curvature at a distance w from the scar line is given by $k(w) = \frac{R(w)}{R(w)^2+T^2}$, where $R(w) = \sqrt{(R-w\sin\beta)^2 + (w\sin\gamma\cos\beta)^2}$. The energy cost to deviate from the flat state, $k(w) =$

0, is then given by

$$\mathcal{E}_{\mathsf{roll}} \sim \int_0^{W_f} k(w)^2 \mathrm{d}w \ . \tag{A.69}$$

Finally, we assign an energy cost to splaying of the grooves. Neighbouring grooves have a preferred constant distance λ. When attached to a helical scar line, their distance d varies with the length w away from the scar line. Defining a splay strain as $\epsilon(w) = \frac{d(w)-\lambda}{\lambda}$, we find a splay energy

$$\mathcal{E}_{\mathsf{splay}} \sim \frac{1}{\lambda^2} \int_0^{W_f} \epsilon(w)^2 \mathrm{d}w \ . \tag{A.70}$$

$$\tag{A.71}$$

Here, we assume that deformations that produce splaying take place over distances of order λ. For completeness, the distance $d(w)$ between neighbouring grooves attached to a scar line with radius of curvature R and pitch $2\pi T$ is given by

$$d^2(w) = T^2t^2 + 2(1-\cos t)(R^2 - w^2(1 - \frac{R^2}{R^2+T^2}\cos^2\beta)) - 2Rw\sin\beta \tag{A.72}$$

where t is defined via ${s_\lambda}^2 = T^2t^2 + 2R^2(1-\cos t)$. While this expression is complex, we hypothesize that the exact mathematical form of the splay strain is not crucial, as long as non-zero splay is penalized.

Thus, the total energy is given by:

$$\mathcal{E}_{\mathsf{tot}} = \mathcal{E}_k + \mathcal{E}_g + \mathcal{E}_\beta + K(\mathcal{E}_{\mathsf{splay}} + \mathcal{E}_{\mathsf{roll}}) \ , \tag{A.73}$$

where $K = 0.1$ is a factor that we choose heuristically. Experience suggests that the scar line is stiffer against deformations than the remainder of the sheet, which we take into account via K, by penalizing sheet deformations less than scar line deformations.

In short: we have defined energetic terms corresponding to deformations of the scar line and groovy sheet. We may now calculate the minimal-energy configurations of such a sheet, given the equilibrium parameters k^0, λ, s_λ, and β^0 for the scar curvature, groove wavelength, groove arc length, and scar folding angle estimated above, using the degree of freedom K to tune the relative cost of scar line versus sheet deformations.

We calculate equilibrium sheet shapes with a custom Python script, which numerically finds a local energetic minimum in the sheet shape parameter space. The resulting shapes are illustrated in Fig. A.11b for short, intermediate, and long widths. Sheet shapes match experimental observations well: narrow sheets roll, while wide sheets twist. Fig. A.11c shows how the sheet shape parameters vary with the sheet width W_f. The shape parameters show qualitative agreement with experimentally observed shapes (Fig. 5.40). First, the rolling radius R starts at an initial, nonzero value at $W_f = 0$, and subsequently increases with W_f. Experiments show that the rolling radius reaches a plateau; this feature is not reproduced by our model, which we attribute to the absence of groove bending in our theory. Secondly, the scar folding angle β lies near its equilibrium value. Lastly, the twisting parameter T undergoes a bifurcation at some critical value of W_f. The energy of the corresponding configurations increases monotonically with W_f.

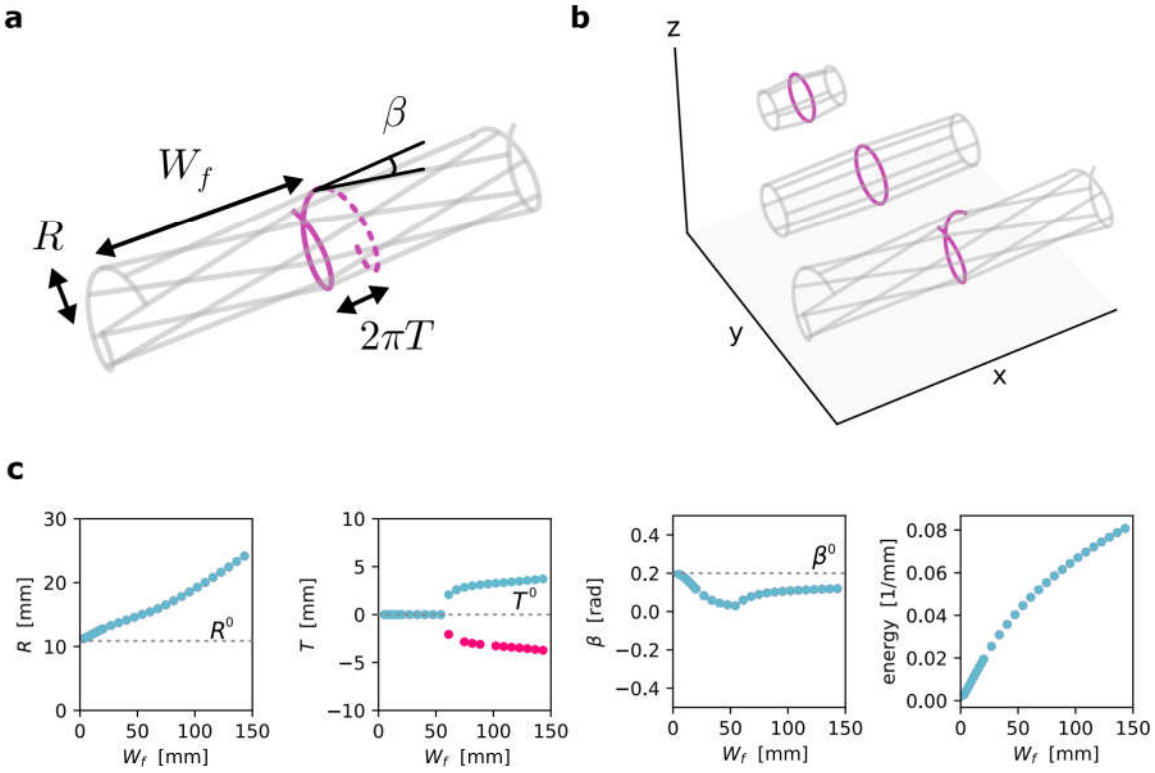

Fig. A.11.: Twisting transition in a simple elastic model. a, Sheets are modelled as ruled surfaces. The scar line forms a helical directrix (pink line) with radius of curvature R and wavelength $2\pi T$. Grooves (grey lines) are approximated as straight lines of length W_f, pointing orthogonally away from the scar line at a small angle β. **b,** Equilibrium configurations of the model at increasing edge width W_f (see text for details). Scar lines are either circular or helicoidal; grooves point away from the scar line at a small angle and exhibit twisting at large W_f. **c,** Equilibrium shape parameters and energy are shown as a function of W_f. The scar rolling radius R increases from its initial value R^0 (Eq. 5.33) with W_f. Initially, the sheet does not twist; at a critical value of W_f, a bifurcation to finite twisting is observed. The angle β at which grooves point away from the scars initially decreases with W_f, but approaches its initial value once more as W_f increases. The total equilibrium energy per sheet section increases monotonically. Initial values R^0, T^0, and β^0 are indicated by dashed grey lines throughout.

In conclusion: despite the need for manual tuning of the relative stiffnesses of scar and sheet, our model suggests that an energetic competition (between twisting deformations of the scar and splaying in the sheet) yields a twisting bifurcation at finite sheet width, consistent with experimental observations.

Bibliography

[1] J. T. B. Overvelde, T. Kloek, J. J. A. D'haen, and K. Bertoldi. "Amplifying the response of soft actuators by harnessing snap-through instabilities". In: *Proceedings of the National Academy of Sciences* 112.35 (2015), pp. 10863–10868.

[2] X. Shang, L. Liu, A. Rafsanjani, and D. Pasini. "Durable bistable auxetics made of rigid solids". In: *Journal of Materials Research* 33.3 (2018), pp. 300–308.

[3] F. Ilievski et al. "Soft Robotics for Chemists". In: *Angewandte Chemie International Edition* 50.8 (2011), pp. 1890–1895.

[4] M. Marder, R. D. Deegan, and E. Sharon. "Crumpling, buckling, and crackling: Elasticity of thin sheets". In: *Physics Today* 60.2 (2007), pp. 33–38.

[5] M. Pezzulla, G. P. Smith, P. Nardinocchi, and D. P. Holmes. "Geometry and mechanics of thin growing bilayers". In: *Soft Matter* 12.19 (2016), pp. 4435–4442.

[6] M. Pezzulla et al. "Curvature-Induced Instabilities of Shells". In: *Physical Review Letters* 120.4 (2018), p. 048002.

[7] C. Coulais et al. "Combinatorial design of textured mechanical metamaterials". In: *Nature* 535.7613 (2016), pp. 529–532.

[8] L. H. Dudte, E. Vouga, T. Tachi, and L. Mahadevan. "Programming curvature using origami tessellations". In: *Nature Materials* 15.5 (2016), pp. 583–588.

[9] C. Coulais, A. Sabbadini, F. Vink, and M. van Hecke. "Multi-step self-guided pathways for shape-changing metamaterials". In: *Nature* 561.7724 (2018), pp. 512–515.

[10] T. Frenzel, M. Kadic, and M. Wegener. "Three-dimensional mechanical metamaterials with a twist". In: *Science* 358.6366 (2017), pp. 1072–1074.

[11] F. G. Broeren, W. W. van de Sande, V. van der Wijk, and J. L. Herder. "A general method for the creation of dilational surfaces". In: *Nature Communications* 10.1 (2019).

[12] N. P. Bende et al. "Overcurvature induced multistability of linked conical frusta: how a 'bendy straw' holds its shape". In: *Soft Matter* 14.42 (2018), pp. 8636–8642.

[13] A. S. Meeussen, E. C. Oğuz, Y. Shokef, and M. L. van Hecke. "Topological defects produce exotic mechanics in complex metamaterials". In: *Nature Physics* 16.3 (2020), pp. 307–311.

[14] A. S. Meeussen, E. C. Oğuz, M. L. van Hecke, and Y. Shokef. "Response evolution of mechanical metamaterials under architectural transformations". In: *New Journal of Physics* 22.2 (2020), p. 23030.

[15] T. Mullin, S. Deschanel, K. Bertoldi, and M. C. Boyce. "Pattern transformation triggered by deformation". In: *Physical Review Letters* 99.8 (2007), pp. 1–4.

[16] B. G.-g. Chen et al. "Topological Mechanics of Origami and Kirigami". In: *Physical Review Letters* 116.13 (2016), pp. 1–5.

[17] J. Paulose, B. G.-g. Chen, and V. Vitelli. "Topological modes bound to dislocations in mechanical metamaterials". In: *Nat. Phys.* 11.2 (2015), pp. 153–156.

[18] J. Paulose, A. S. Meeussen, and V. Vitelli. "Selective buckling via states of self-stress in topological metamaterials". In: *Proceedings of the National Academy of Sciences* 112.25 (2015), pp. 7639–7644.

[19] M. Serra-Garcia et al. "Observation of a phononic quadrupole topological insulator". In: *Nature* 555.7696 (2018), pp. 342–345.

[20] B. Florijn, C. Coulais, and M. van Hecke. "Programmable Mechanical Metamaterials". In: *Physical Review Letters* 113.17 (2014), p. 175503.

[21] K. Bertoldi, V. Vitelli, J. Christensen, and M. van Hecke. "Flexible mechanical metamaterials". In: *Nature Reviews Materials* 2.11 (2017), p. 17066.

[22] S. H. Kang et al. "Complex ordered patterns in mechanical instability induced geometrically frustrated triangular cellular structures". In: *Physical Review Letters* 112.9 (2014), pp. 1–5.

[23] C. Nisoli, R. Moessner, and P. Schiffer. "Colloquium: Artificial spin ice: Designing and imaging magnetic frustration". In: *Rev. Mod. Phys.* 85.4 (2013), pp. 1473–1490.

[24] R. F. Wang et al. "Artificial 'spin ice' in a geometrically frustrated lattice of nanoscale ferromagnetic islands". In: *Nature* 439.7074 (2006), pp. 303–306.

[25] C. Castelnovo, R. Moessner, and S. L. Sondhi. "Magnetic monopoles in spin ice". In: *Nature* 451.7174 (2008), pp. 42–45.

[26] N. D. Mermin. "The topological theory of defects in ordered media". In: *Rev. Mod. Phys.* 51.3 (1979), pp. 591–648.

[27] G. P. Alexander, B. G.-g. Chen, E. A. Matsumoto, and R. D. Kamien. "Colloquium: Disclination loops, point defects, and all that in nematic liquid crystals". In: *Rev. Mod. Phys.* 84.2 (2012), pp. 497–514.

[28] J. N. Grima, A Alderson, and K. E. Evans. "Auxetic behaviour from rotating rigid units". In: *Phys. Status Solidi B* 242.3 (2005), pp. 561–575.

[29] C. Coulais, C. Kettenis, and M. Van Hecke. "A characteristic length scale causes anomalous size effects and boundary programmability in mechanical metamaterials". In: *Nature Physics* 14.1 (2018), pp. 40–44.

[30] R. M. A. Zandbergen. "On the Number of Configurations of Triangular Mechanisms". Bachelor's Thesis. Leiden University, 2016.

[31] M. J. Morrison, T. R. Nelson, and C. Nisoli. "Unhappy vertices in artificial spin ice: new degeneracies from vertex frustration". In: *New Journal of Physics* 15.4 (2013), p. 045009.

[32] I. Syôzi. "Statistics of Kagomé Lattice". In: *Prog. Theor. Phys.* 6.3 (1951), pp. 306–308.

[33] K. Kano and S. Naya. "Antiferromagnetism. The Kagomé Ising net". In: *Prog. Theor. Phys.* 10.2 (1953), pp. 158–172.

[34] K. Bertoldi, P. M. Reis, S. Willshaw, and T. Mullin. "Negative poisson's ratio behavior induced by an elastic instability". In: *Advanced Materials* 22.3 (2010), pp. 361–366.

[35] G.-W. Chern and O. Tchernyshyov. "Magnetic charge and ordering in kagome spin ice". In: *Philosophical Transactions of the Royal Society A: Mathematical, Physical and Engineering Sciences* 370.1981 (2012), pp. 5718–5737.

[36] M. O. Blunt et al. "Random Tiling and Topological Defects in a Two-Dimensional Molecular Network". In: *Science* 322.5904 (2008), pp. 1077–1081.

[37] P. A. MacMahon. *Combinatory Analysis*. Vol. 2. London: Cambridge University Press, 1916.

[38] N. J. A. Sloane. *The On-Line Encyclopedia of Integer Sequences*. 1996. URL: https://oeis.org/A008793.

[39] E. T. Filipov, T. Tachi, and G. H. Paulino. "Origami tubes assembled into stiff, yet reconfigurable structures and metamaterials". In: *Proceedings of the National Academy of Sciences* 112.40 (2015), pp. 12321–12326.

[40] S. Gaitanaros, S. Kyriakides, and A. M. Kraynik. "On the crushing response of random open-cell foams". In: *International Journal of Solids and Structures* 49.19-20 (2012), pp. 2733–2743.

[41] G. Toulouse. "Theory of the frustration effect in spin glasses: I". In: *Commun. Phys.* 2 (1977), pp. 115–119.

[42] A. Ortiz-Ambriz and P. Tierno. "Engineering of frustration in colloidal artificial ices realized on microfeatured grooved lattices". In: *Nature Communications* 7.1 (2016), p. 10575.

[43] C. Nisoli, V. Kapaklis, and P. Schiffer. "Deliberate exotic magnetism via frustration and topology". In: *Nature Physics* 13.3 (2017), pp. 200–203.

[44] C. L. Kane and T. C. Lubensky. "Topological boundary modes in isostatic lattices". In: *Nature Physics* 10.1 (2013), pp. 39–45.

[45] Y. Lao et al. "Classical topological order in the kinetics of artificial spin ice". In: *Nature Physics* 14.July (2018), pp. 723–728.

[46] R. J. Lang. *Origami In Action: Paper Toys That Fly, Flag, Gobble and Inflate!* St. Martin's Publishing Group, 1997.

[47] M. A. Bessa, P. Glowacki, and M. Houlder. "Bayesian Machine Learning in Metamaterial Design: Fragile Becomes Supercompressible". In: *Advanced Materials* 31.48 (2019), p. 1904845.

[48] M. P. Bendsøe and O. Sigmund. *Topology optimization: theory, methods, and applications*. New York: Springer, 2004.

[49] N. Singh and M. van Hecke. "Design of pseudo-mechanisms and multistable units for mechanical metamaterials". 2020. URL: http://arxiv.org/abs/2003.11239.

[50] C. Schumacher et al. "Microstructures to control elasticity in 3D printing". In: *ACM Transactions on Graphics* 34.4 (2015), 136:1–136:13.

[51] M. Kadic, T. Bückmann, R. Schittny, and M. Wegener. "Metamaterials beyond electromagnetism". In: *Reports on Progress in Physics* 76.12 (2013), p. 126501.

[52] S. sp. z o.o. *Sinterit LISA product specification*. 2014. URL: https://www.sinterit.com/wp-content/uploads/2014/05/LISA_Specification.pdf.

[53] S. sp. z o.o. *Sinterit Flexa Black specification*. 2014. URL: https://www.sinterit.com/wp-content/uploads/2014/05/Flexa-Black-Specification.pdf.

[54] S. Pellegrino and C. Calladine. "Matrix analysis of statically and kinematically indeterminate frameworks". In: *International Journal of Solids and Structures* 22.4 (1986), pp. 409–428.

[55] S. Pellegrino. "Structural computations with the singular value decomposition of the equilibrium matrix". In: *International Journal of Solids and Structures* 30.21 (1993), pp. 3025–3035.

[56] B. Audoly and Y. Pomeau. *Elasticity and Geometry.* New York: Oxford University Press, 2010.

[57] ISO. *ISO 37:2017 Rubber, vulcanized or thermoplastic — Determination of tensile stress-strain properties.* 2017.

[58] D. Mousanezhad et al. "Hierarchical honeycomb auxetic metamaterials". In: *Scientific Reports* 5 (2015), p. 18306.

[59] B. Liu et al. "Topological kinematics of origami metamaterials". In: *Nat. Phys.* 14.August (2018), pp. 1–5.

[60] X. Ning et al. "Assembly of advanced materials into 3D functional structures by methods inspired by origami and kirigami: A review". In: *Adv. Mater. Interfaces* 5.13 (2018), pp. 1–13.

[61] M. A. McEvoy and N Correll. "Materials that couple sensing, actuation, computation, and communication". In: *Science* 347.6228 (2015), p. 1261689.

[62] P. M. Reis, H. M. Jaeger, and M. Van Hecke. "Designer matter: A perspective". In: *Extreme Mech. Lett.* 5 (2015), pp. 25–29.

[63] M. Wehner et al. "An integrated design and fabrication strategy for entirely soft, autonomous robots". In: *Nature* 536.7617 (2016), pp. 451–455.

[64] J. T. Overvelde et al. "A three-dimensional actuated origami-inspired transformable metamaterial with multiple degrees of freedom". In: *Nature Communications* 7 (2016), pp. 1–8.

[65] J. L. Silverberg et al. "Using origami design principles to fold reprogrammable mechanical metamaterials". In: *Science* 345.6197 (2014), pp. 647–650.

[66] P. Celli et al. "Shape-morphing architected sheets with non-periodic cut patterns". In: *Soft Matter* 14.48 (2018), pp. 9744–9749.

[67] N. W. Bartlett et al. "A 3D-printed, functionally graded soft robot powered by combustion". In: *Science* 349.6244 (2015), pp. 161–165.

[68] R. S. Lakes. "Foam structures with a negative Poisson's ratio". In: *Science* 235 (1987), pp. 1038–1040.

[69] M. Kadic et al. "On the practicability of pentamode mechanical metamaterials". In: *Applied Physics Letters* 100.19 (2012), p. 191901.

[70] A. Libál, C. Reichhardt, and C. J. O. Reichhardt. "Realizing Colloidal Artificial Ice on Arrays of Optical Traps". In: *Physical Review Letters* 97.22 (2006), p. 228302.

[71] Y. Han et al. "Geometric frustration in buckled colloidal monolayers". In: *Nature* 456.7224 (2008), pp. 898–903.

[72] Y. Shokef, A. Souslov, and T. C. Lubensky. "Order by disorder in the antiferromagnetic Ising model on an elastic triangular lattice". In: *Proceedings of the National Academy of Sciences* 108.29 (2011), pp. 11804–11809.

[73] F. Leoni and Y. Shokef. “Attraction Controls the Inversion of Order by Disorder in Buckled Colloidal Monolayers”. In: *Physical Review Letters* 118.21 (2017), p. 218002.

[74] J. N. Grima and K. E. Evans. “Auxetic behavior from rotating squares”. In: *Journal of Materials Science Letters* 19.17 (2000), pp. 1563–1565.

[75] W. G. Ellenbroek, Z. Zeravcic, W. van Saarloos, and M. van Hecke. “Non-affine response: Jammed packings vs. spring networks”. In: *EPL (Europhysics Letters)* 87.3 (2009), p. 34004.

[76] W. G. Ellenbroek et al. “Rigidity Loss in Disordered Systems: Three Scenarios”. In: *Physical Review Letters* 114.13 (2015), p. 135501.

[77] C. P. Goodrich, A. J. Liu, and S. R. Nagel. “The Principle of Independent Bond-Level Response: Tuning by Pruning to Exploit Disorder for Global Behavior”. In: *Physical Review Letters* 114.22 (2015), p. 225501.

[78] J. W. Rocks et al. “Designing allostery-inspired response in mechanical networks”. In: *Proceedings of the National Academy of Sciences* 114.10 (2017), pp. 2520–2525.

[79] D. M. Sussman, C. P. Goodrich, and A. J. Liu. “Spatial structure of states of self stress in jammed systems”. In: *Soft Matter* 12.17 (2016), pp. 3982–3990.

[80] D. Hexner, A. J. Liu, and S. R. Nagel. “Linking microscopic and macroscopic response in disordered solids”. In: *Physical Review E* 97.6 (2018), p. 063001.

[81] D. Hexner, A. J. Liu, and S. R. Nagel. “Role of local response in manipulating the elastic properties of disordered solids by bond removal”. In: *Soft Matter* 14.2 (2018), pp. 312–318.

[82] D. S. Bassett et al. “Extraction of force-chain network architecture in granular materials using community detection”. In: *Soft Matter* 11.14 (2015), pp. 2731–2744.

[83] S. D. Guest and J. W. Hutchinson. “On the determinacy of repetitive structures”. In: *Journal of the Mechanics and Physics of Solids* 51.3 (2003), pp. 383–391.

[84] J. C. Maxwell. “On the calculation of the equilibrium and stiffness of frames”. In: *The London, Edinburgh, and Dublin Philosophical Magazine and Journal of Science* 27.182 (1864), pp. 294–299.

[85] C. R. Calladine. “Buckminster Fuller’s ”Tensegrity” structures and Clerk Maxwell’s rules for the construction of stiff frames”. In: *International Journal of Solids and Structures* 14.2 (1978), pp. 161–172.

[86] R. Connelly. “Rigidity and energy”. In: *Inventiones Mathematicae* 66.1 (1982), pp. 11–33.

[87] T. C. Lubensky et al. “Phonons and elasticity in critically coordinated lattices”. In: *Reports on Progress in Physics* 78.7 (2015), pp. 1–38.

[88] G. H. Wannier. “Antiferromagnetism. The Triangular Ising Net”. In: *Physical Review* 79.2 (1950), pp. 357–364.

[89] E. Lerner. “Quasilocalized states of self stress in packing-derived networks”. In: *European Physical Journal E* 41.8 (2018), pp. 1–8.

[90] F. S. Nascimento, L. A. Mól, W. A. Moura-Melo, and A. R. Pereira. “From confinement to deconfinement of magnetic monopoles in artificial rectangular spin ices”. In: *New Journal of Physics* 14 (2012).

[91] D. Z. Rocklin et al. "Mechanical Weyl Modes in Topological Maxwell Lattices". In: *Physical Review Letters* 116.13 (2016), pp. 1–5.

[92] S. D. Guest and P. W. Fowler. "A symmetry-extended mobility rule". In: *Mechanism and Machine Theory* 40.9 (2005), pp. 1002–1014.

[93] W. Ji et al. "Theory for the density of interacting quasilocalized modes in amorphous solids". In: *Physical Review E* 99.2 (2019), pp. 1–8.

[94] S. Wijtmans and M. Lisa Manning. "Disentangling defects and sound modes in disordered solids". In: *Soft Matter* 13.34 (2017), pp. 5649–5655.

[95] J. H. Snoeijer, T. J. H. Vlugt, M. van Hecke, and W. van Saarloos. "Force Network Ensemble: A New Approach to Static Granular Matter". In: *Physical Review Letters* 92.5 (2004), p. 054302.

[96] K. Ramola and B. Chakraborty. "Stress Response of Granular Systems". In: *Journal of Statistical Physics* 169.1 (2017), pp. 1–17.

[97] G. Lois et al. "Stress correlations in granular materials: An entropic formulation". In: *Physical Review E - Statistical, Nonlinear, and Soft Matter Physics* 80.6 (2009), pp. 1–4.

[98] E. Cerda and L. Mahadevan. "Conical Surfaces and Crescent Singularities in Crumpled Sheets". In: *Physical Review Letters* 80.11 (1998), pp. 2358–2361.

[99] T. A. Witten. "Stress focusing in elastic sheets". In: *Reviews of Modern Physics* 79.2 (2007), pp. 643–675.

[100] S. Conti and F. Maggi. "Confining thin elastic sheets and folding paper". In: *Archive for Rational Mechanics and Analysis* 187.1 (2008), pp. 1–48.

[101] E. Cerda, S. Chaieb, F. Melo, and L. Mahadevan. "Conical dislocations in crumpling". In: *Nature* 401.6748 (1999), pp. 46–49.

[102] T. Jules, F. Lechenault, and M. Adda-Bedia. "Local mechanical description of an elastic fold". In: *Soft Matter* 15.7 (2019), pp. 1619–1626.

[103] H. Kobayashi, B. Kresling, and J. F. V. Vincent. "The geometry of unfolding tree leaves". In: *Proceedings of the Royal Society of London. Series B: Biological Sciences* 265.1391 (1998), pp. 147–154.

[104] E. Couturier, S. Courrech du Pont, and S. Douady. "A Global Regulation Inducing the Shape of Growing Folded Leaves". In: *PLoS ONE* 4.11 (2009). Ed. by S. Humphries, e7968.

[105] K. A. Seffen. "Compliant shell mechanisms". In: *Philosophical Transactions of the Royal Society A: Mathematical, Physical and Engineering Sciences* 370.1965 (2012), pp. 2010–2026.

[106] V. Brunck, F. Lechenault, A. Reid, and M. Adda-Bedia. "Elastic theory of origami-based metamaterials". In: *Physical Review E - Statistical, Nonlinear, and Soft Matter Physics* 93.3 (2016), pp. 1–14.

[107] A. Norman, K. Seffen, and S. Guest. "Morphing of curved corrugated shells". In: *International Journal of Solids and Structures* 46.7-8 (2009), pp. 1624–1633.

[108] B. Audoly and Y. Pomeau. *Elasticity and Geometry.* New York: Oxford University Press, 2010.

[109] K. F. Gauss. *General Investigations of Curved Surfaces*. Ed. by P. Pesic. Princeton: Princeton University Library, 1992.

[110] V Pini et al. "How two-dimensional bending can extraordinarily stiffen thin sheets". In: *Scientific Reports* 6.1 (2016), p. 29627.

[111] E. Kebadze, S. D. Guest, and S. Pellegrino. "Bistable prestressed shell structures". In: *International Journal of Solids and Structures* 41.11-12 (2004), pp. 2801–2820.

[112] M. Pignataro, N. Rizzi, and A. Luongo. *Stability, bifurcation and postcritical behaviour of elastic structures*. Amsterdam: Elsevier Science Publishers B.V., 1991.

[113] N. Oppenheimer and T. A. Witten. "Shapeable sheet without plastic deformation". In: *Physical Review E - Statistical, Nonlinear, and Soft Matter Physics* 92.5 (2015), pp. 1–14.

[114] J. L. Silverberg et al. "Origami structures with a critical transition to bistability arising from hidden degrees of freedom." In: *Nat. Mater.* 14.4 (2015), pp. 389–393.

[115] S. Waitukaitis, R. Menaut, B. G.-g. Chen, and M. van Hecke. "Origami Multistability: From Single Vertices to Metasheets". In: *Physical Review Letters* 114.5 (2015), p. 055503.

[116] A. Pandey, D. E. Moulton, D. Vella, and D. P. Holmes. "Dynamics of snapping beams and jumping poppers". In: *EPL (Europhysics Letters)* 105.2 (2014), p. 24001.

[117] K. Seffen, B Wang, and S. Guest. "Folded orthotropic tape-springs". In: *Journal of the Mechanics and Physics of Solids* 123 (2019), pp. 138–148.

[118] A. Norman, K. Seffen, and S. Guest. "Multistable corrugated shells". In: *Proceedings of the Royal Society A: Mathematical, Physical and Engineering Sciences* 464.2095 (2008), pp. 1653–1672.

[119] M. G. Walker. "Mechanics of generically creased disks". In: *Physical Review E* 101.4 (2020), p. 43001.

[120] Y. Forterre, J. M. Skotheim, J. Dumals, and L. Mahadevan. "How the Venus flytrap snaps". In: *Nature* 433.7024 (2005), pp. 421–425.

[121] T. Savin et al. "On the growth and form of the gut". In: *Nature* 476.7358 (2011), pp. 57–62.

[122] H. Liang and L. Mahadevan. "Growth, geometry, and mechanics of a blooming lily". In: *Proceedings of the National Academy of Sciences* 108.14 (2011), pp. 5516–5521.

[123] A. Vaziri. "Mechanics of highly deformed elastic shells". In: *Thin-Walled Structures* 47.6-7 (2009), pp. 692–700.

[124] A. Nasto et al. "Localization of deformation in thin shells under indentation". In: *Soft Matter* 9.29 (2013), p. 6796.

[125] M. Das, A. Vaziri, A. Kudrolli, and L. Mahadevan. "Curvature Condensation and Bifurcation in an Elastic Shell". In: *Physical Review Letters* 98.1 (2007), p. 014301.

[126] L. Walsh, R. Meza, and E. Hamm. "Weakening of a thin shell structure by annihilating singularities". In: *Journal of Physics D: Applied Physics* 44.23 (2011), p. 232002.

[127] N. P. Bende et al. "Geometrically controlled snapping transitions in shells with curved creases". In: *Proceedings of the National Academy of Sciences of the United States of America* 112.36 (2015), pp. 11175–11180.

[128] J. P. Udani and A. F. Arrieta. "Programmable mechanical metastructures from locally bistable domes". In: *Extreme Mechanics Letters* (2020), p. 101081.

[129] T. Tallinen, J. Ojajärvi, J. A. Åström, and J. Timonen. "Scaling Behavior in Non-Hookean Compression of Thin-Walled Structures". In: *Physical Review Letters* 105.6 (2010), p. 066102.

[130] E. Efrati, E. Sharon, and R. Kupferman. "Elastic theory of unconstrained non-Euclidean plates". In: *Journal of the Mechanics and Physics of Solids* 57.4 (2009), pp. 762–775.

[131] M. Lewicka, L. Mahadevan, and M. R. Pakzad. "The Föppl-von Kármán equations for plates with incompatible strains". In: *Proceedings of the Royal Society A: Mathematical, Physical and Engineering Sciences* 467.2126 (2011), pp. 402–426.

[132] T. J. Healey, Q. Li, and R.-B. Cheng. "Wrinkling Behavior of Highly Stretched Rectangular Elastic Films via Parametric Global Bifurcation". In: *Journal of Nonlinear Science* 23.5 (2013), pp. 777–805.

[133] M. A. Dias and B. Audoly. ""Wunderlich, Meet Kirchhoff": A General and Unified Description of Elastic Ribbons and Thin Rods". In: *Journal of Elasticity* 119.1-2 (2015), pp. 49–66.

[134] A. P. Korte, E. L. Starostin, and G. H. M. van der Heijden. "Triangular buckling patterns of twisted inextensible strips". In: *Proceedings of the Royal Society A: Mathematical, Physical and Engineering Sciences* 467.2125 (2011), pp. 285–303.

[135] E. Fried. *The Mechanics of Ribbons and Möbius Bands*. Ed. by R. Fosdick and E. Fried. Dordrecht: Springer Netherlands, 2016, pp. 35–48.

[136] M. A. Dias and B. Audoly. "A non-linear rod model for folded elastic strips". In: *Journal of the Mechanics and Physics of Solids* 62.1 (2014), pp. 57–80.

[137] H. Olbermann. "The shape of low energy configurations of a thin elastic sheet with a single disclination". In: *Analysis & PDE* 11.5 (2018), pp. 1285–1302.

[138] K. A. Seffen. "Fundamental conical defects: The d-cone, its e-cone, and its p-cone". In: *Physical Review E* 94.1 (2016), p. 013002.

[139] J. Genzer and J. Groenewold. "Soft matter with hard skin: From skin wrinkles to templating and material characterization". In: *Soft Matter* 2.4 (2006), p. 310.

[140] H. Vandeparre et al. "Wrinkling hierarchy in constrained thin sheets from suspended graphene to curtains". In: *Physical Review Letters* 106.22 (2011), pp. 2–5.

[141] J. Hure, B. Roman, and J. Bico. "Stamping and Wrinkling of Elastic Plates". In: *Physical Review Letters* 109.5 (2012), p. 054302.

[142] B. Li, Y.-P. Cao, X.-Q. Feng, and H. Gao. "Mechanics of morphological instabilities and surface wrinkling in soft materials: a review". In: *Soft Matter* 8.21 (2012), p. 5728.

[143] E. Sharon, B. Roman, and H. L. Swinney. "Geometrically driven wrinkling observed in free plastic sheets and leaves". In: *Physical Review E - Statistical, Nonlinear, and Soft Matter Physics* 75.4 (2007), pp. 1–7.

[144] H. Liang and L Mahadevan. “The shape of a long leaf”. In: *Proceedings of the National Academy of Sciences* 106.52 (2009), pp. 22049–22054.

[145] W. H. Frey. “Modeling buckled developable surfaces by triangulation”. In: *Computer-Aided Design* 36.4 (2004), pp. 299–313.

[146] Z. Y. Wei et al. “Geometric Mechanics of Periodic Pleated Origami”. In: *Physical Review Letters* 110.21 (2013), p. 215501.

[147] B. L. Wardle. “Impact and Quasi-Static Response of Cylindrical Composite Shells”. In: (1992).

[148] K. A. Seffen. “On the Behavior of Folded Tape-Springs”. In: *Journal of Applied Mechanics* 68.3 (2001), pp. 369–375.

[149] M. G. Walker and K. A. Seffen. “On the shape of bistable creased strips”. In: *Thin-Walled Structures* 124 (2018), pp. 538–545.

[150] DuPont Teijin Films. *Mylar ® polyester film: physical-thermal properties*. 2003.

[151] S. P. Timoshenko. *History of strength of materials*. New York: Dover Publications, Inc., 1983.

[152] Zhermack S.p.A. *Elite Double vinylpolysiloxane (addition silicone) duplicating material*. 2016.

[153] A. N. Gent. “On the Relation between Indentation Hardness and Young’s Modulus”. In: *Rubber Chemistry and Technology* 31.4 (1958), pp. 896–906.

[154] D. G. Van Velzen. “Elastic Moduli of Smooth and Corrugated Thin Silicone Rubber”. MSc thesis. Leiden University, 2017.

[155] S. Van der Jeught, J. A. M. Soons, and J. J. J. Dirckx. “Real-time microscopic phase-shifting profilometry”. In: *Applied Optics* 54.15 (2015), p. 4953.

[156] S. Wildeman. “Real-time quantitative Schlieren imaging by fast Fourier demodulation of a checkered backdrop”. In: *Experiments in Fluids* 59.6 (2018), p. 97.

[157] P. S. Huang. “Novel method for structured light system calibration”. In: *Optical Engineering* 45.8 (2006), p. 083601.

[158] J. E. Gordon. *Structures , or Why Things Don’t Fall Down*. Cambridge: Da Capo Press, 2003.

[159] T. G. Hicks. *Civil Engineering Formulas*. 2nd ed. New York: McGraw-Hill, 2010.

[160] F. Lechenault, B. Thiria, and M. Adda-Bedia. “Mechanical Response of a Creased Sheet”. In: *Physical Review Letters* 112.24 (2014), p. 244301.

[161] Wolfram Research Inc. *Mathematica, version 11.2*. Champaign, IL, 2020.

[162] C. D. Santangelo. “Nambu–Goldstone modes and diffuse deformations in elastic shells”. In: *Soft Matter* 9.34 (2013), p. 8246.

[163] A. Vaziri and L Mahadevan. “Localized and extended deformations of elastic shells”. In: *Proceedings of the National Academy of Sciences* 105.23 (2008), pp. 7913–7918.

[164] R. D. Schroll, E. Katifori, and B. Davidovitch. “Elastic Building Blocks for Confined Sheets”. In: *Physical Review Letters* 106.7 (2011), p. 074301.

[165] B. Roman and A. Pocheau. “Stress Defocusing in Anisotropic Compaction of Thin Sheets”. In: *Physical Review Letters* 108.7 (2012), p. 074301.

[166] T. Barois, L. Tadrist, C. Quilliet, and Y. Forterre. "How a Curved Elastic Strip Opens". In: *Physical Review Letters* 113.21 (2014), p. 214301.

[167] C. Keplinger et al. "Stretchable, transparent, ionic conductors". In: *Science* 341.6149 (2013), pp. 984–987.

[168] J.-Y. Sun et al. "Highly stretchable and tough hydrogels". In: *Nature* 489.7414 (2012), pp. 133–136.

[169] DuPont Teijin Films. *Mylar ® polyester film: introduction*. 2003.

[170] ASTM. "D 882: Standard Test Method for Tensile Properties of Thin Plastic Sheeting". In: *Astm* 14 (2002), pp. 1–10.

[171] Instron. *Instron 3360 Series*. 2015.

[172] Instron. *Instron 2530 Series Static Load Cells*. 2016.

[173] University of Cambridge. *DoITPoMS: bending and torsion of beams*. 2008. URL: `https://www.doitpoms.ac.uk/tlplib/beam_bending/index.php`.

[174] B. Fornberg. "Generation of finite difference formulas on arbitrarily spaced grids". In: *Mathematics of Computation* 51.184 (1988), pp. 699–699.